Eur. J. Mineral., 38, 281–304, 2026
https://doi.org/10.5194/ejm-38-281-2026


European Journal of Mineralogy
Open Access

# Mineralogy of sulfide mineralization from the world-class Li–Sn–W Cínovec greisen-type deposit, Bohemian Massif, Czech Republic

**Ondřej Krátký[1], Jan Cempírek[1], Sebastián Hreus[1,2], Luboš Vrtiška[3], Jiří Sejkora[3], Zdeněk Dolníček[3], Jakub Výravský[1,4], Radek Škoda[1], Karel Breiter[5], and Vojtěch Šešulka[6]**

[1]Faculty of Science, Masaryk University, Kotlářská 2, 602 00 Brno, Czech Republic
[2]Faculty of Mining, Ecology, Process Control and Geotechnology, Technical University of Košice, Letná 9, 04001 Košice, Slovakia
[3]Department of Mineralogy and Petrology, National Museum, Cirkusová 1740, 193 00 Prague 9, Czech Republic
[4]TESCAN GROUP a.s., Libušina třída 21, 623 00 Brno, Czech Republic
[5]Institute of Geology of the CAS, Rozvojová 269, 165 00 Prague 6, Czech Republic
[6]Geomet s.r.o., Mstišov, Školní 299, 417 03 Dubí, Czech Republic

**Correspondence:** Ondřej Krátký (ondra.kratky@gmail.com) and Jan Cempírek (jcemp@sci.muni.cz)

Received: 21 December 2025 – Revised: 12 March 2026 – Accepted: 23 April 2026 – Published: 20 May 2026

**Abstract.** Mineralogical, paragenetic, and geochemical data on sulfidic mineralization from the Cínovec Li–Sn–W greisen-type deposit (Bohemian Massif, Czech Republic) were used to refine the evolution of mineralization at this world-class deposit and to clarify the relationship between base-metal sulfides and the Li–Sn–W mineralization. Sulfides occur in three main settings: (i) quartz–zinnwaldite veins, (ii) massive greisens and greisenized granites, and (iii) late baryte–fluorite veins that locally overprint earlier types. Electron microprobe analyses and detailed BSE imaging reveal multiple mineralization stages and a surprisingly large suite of sulfide minerals. They were divided into several mineralization stages, including the greisen stage (molybdenite, arsenopyrite, safflorite), early sulfide stage (stannite–kësterite, stannoidite, sphalerite), intermediate sulfide stage (galena), and late sulfide stage (pyrite, marcasite, chalcopyrite, tennantite–tetrahedrite, enargite, lautite, Cu–Ag–Bi–Pb sulfosalts, native Bi, Cu sulfides, pearceite, cupropearceite, stromeyerite). A minor amount of sulfides was remobilized during later the fluorite–baryte stage. Distribution of sulfide mineralization at the deposit is irregular; sulfides are not strictly bound to prevalent Li–Sn–W mineralization. The dominant sphalerite-bearing assemblages (Zn–Pb–Cu) display average grades of $\sim$100–200 ppm Zn (however, Zn is partly contained in zinnwaldite), 20–50 ppm Pb, and $<$ 50 ppm Cu in disseminated mineralization, with locally elevated In contents ($\leq$ 0.53 wt %) in sphalerite. Progressive evolution of metal contents in the reduced sulfide-bearing hydrothermal fluid proceeds from Zn–Cu–Sn to Pb–Bi–Ag and As–Sb. Late-stage sulfate- and fluorine-bearing fluids partly altered earlier mineralization but did not deposit significant ore content.

## 1 Introduction

Cínovec/Zinnwald is a world-class greisen-type Li, Sn, and W deposit, with elevated contents of Nb, Ta, Rb, and Sc. It is situated in the uppermost part of the granite cupola (approximately 1.4 km × 0.3 km in size) at the Czech–German border in the Krušné hory/Erzgebirge. The mineralization is represented especially by Li-bearing micas, cassiterite, wolframite, and minor scheelite. Besides fluorite and topaz, important accessory phases include zircon, Nb-rich rutile, xenotime, columbite, monazite, Sc-rich ixiolite, and pyrochlore (Johan and Johan, 1994, 2005; Breiter et al., 2017a, b, c; Hreus et al., 2021).

The deposit belongs to one of the oldest tin producers in Central Europe; the first evidence of cassiterite mining is dated to 1378, but cassiterite extraction from stream sediments in the whole district (Krupka, Fürstenwalde and Altenberg deposits) was carried out much earlier. Since the 14th century, approximately 8–10 Mt of Sn + W ore was excavated by underground workings, mainly from flat-lying quartz–zinnwaldite veins (so-called "flötze") with coarse-grained cassiterite + wolframite mineralization (Breiter et al., 2016).

In the Krušné hory/Erzgebirge (further simplified as "Erzgebirge"), there is a full range of transitions from (almost) sulfide-free Sn–W deposits (e.g., Cínovec/Zinnwald), through sulfide-enriched deposits (Sn–W in greisen, sulfides in veins mainly in exocontact like Krupka–Knöttl; Žák, 1966; Sejkora and Breiter, 1999; Pauliš et al., 2022) to sulfide-rich deposits with a small amount of cassiterite and missing W, e.g., Hora Sv. Kateřiny and Hora Sv. Šebestiána (Breiter et al., 2009a). Other localities with Sn–W mineralization with variable sulfide content are Krupka, Hrob–Mikulov, and Preissleberg on the Czech side and Altenberg, Sadisdorf, and Sachsenhöhe on the German side (Leopardi et al., 2024).

In the 2010s, exploration programs of the Czech and German parts of the Cínovec/Zinnwald deposit provided large amounts of new data and material. This allowed examination of sulfide mineralization and its extent, mineralogy, and economic importance. In this paper we summarize results from the Czech part (Cínovec deposit), based on samples kindly provided by Geomet s.r.o., and samples collected during the deposit operation stored in the collection of the National Museum in Prague.

## 2 Geological setting

The NE–SW trending crystalline belt of the Erzgebirge is located along the Czech–German border (Fig. 1), within the Saxo-Thuringian Zone of the Bohemian Massif (Hoth et al., 1995; Linnemann, 2008; Cháb et al., 2010). The Saxo-Thuringian Zone contains the geological record of two orogeneses that are separated by a period of crustal extension and marine sedimentation (Linnemann, 2008). The oldest known basement is represented by Neoproterozoic–Cambrian greywackes deposited on the northern peri-Gondwana shelf. This complex was deformed, metamorphosed in amphibolite facies, and finally intruded with granitoids during Cadomian orogeny at 570–540 Ma. Following the Lower and Middle Ordovician, sediments were deposited in a rift setting at the southern margin of the Rheic Ocean (Linnemann and Romer, 2010). Sedimentation follows up to the Devonian, but these younger sequences are not represented in the Erzgebirge. Variscan deformation started in the Upper Devonian by NE- to SW-directed convergence. The locally found UHT rocks (granulites) and UHP ultrabasic rocks with diamonds (Kotková et al., 2011) record final Gondwana subduction below the allochthonous units at 340 Ma. Extensive Variscan post-kinematic magmatism evolved from ca. 330 to 310 Ma, i.e., to the late Carboniferous, with only sporadic continuation to the early Permian (295 Ma at Gottesberg, western Erzgebirge; Förster et al., 2007).

The axis of the Erzgebirge anticlinorium dips towards the southwest so that three distinct stratigraphic units outcrop on actual surface from NE to SW: Proterozoic gneisses in the northeast, upper Proterozoic, and Cambrian mica schists in the center and Ordovician phyllites and quartzites in the southwest. All these units are intruded by late Carboniferous granitoids.

The Variscan granites of the Erzgebirge region should be divided into two major geochemical suites (Fig. 1):

a. Strongly peraluminous granites (A/CNK = 1.1–1.3). These are typical S-type granites with a trend marked by enrichment in P, Na, F, Li, Sn, and U and depletion in Mg, Ca, HREE, and HFSE (like Zr and Th). These granites formed relatively large, deeply eroded plutons in the western part of the Erzgebirge including composite Nejdek–Eibenstock pluton (323–314 Ma; Tichomirowa et al., 2019) and some minor, mostly hidden bodies in the central part of the Erzgebirge (Satzung, Pobershau, Hora sv. Šebestiána).

b. Slightly peraluminous granites (A/CNK = 1.0–1.1). These granites have very low P and high Na, F, Li, REE, and HFSE, often associated with subvolcanic to volcanic activity. These granites, which are a rather rare type among the European Variscan granitoids, can be classified as A-type granites (Breiter, 2012). The largest magmatic system of this type is the Altenberg–Teplice Caldera (18 × 35 km in size), situated in the eastern Erzgebirge and hosting the Cínovec/Zinnwald deposit. Several effusive–intrusive phases can be distinguished within the caldera (Breiter, 1997; Müller et al., 2005), namely (1) three pulses of Teplice rhyolite tuffs and ignimbrites and (2) dikes of granite porphyry related to caldera collapse (312 Ma; Tomek et al., 2019). The volcanic rocks were intruded by two types of granites of distinct geochemical A-type character: (3) the multiple intrusion of the Preiselberg granite formed a

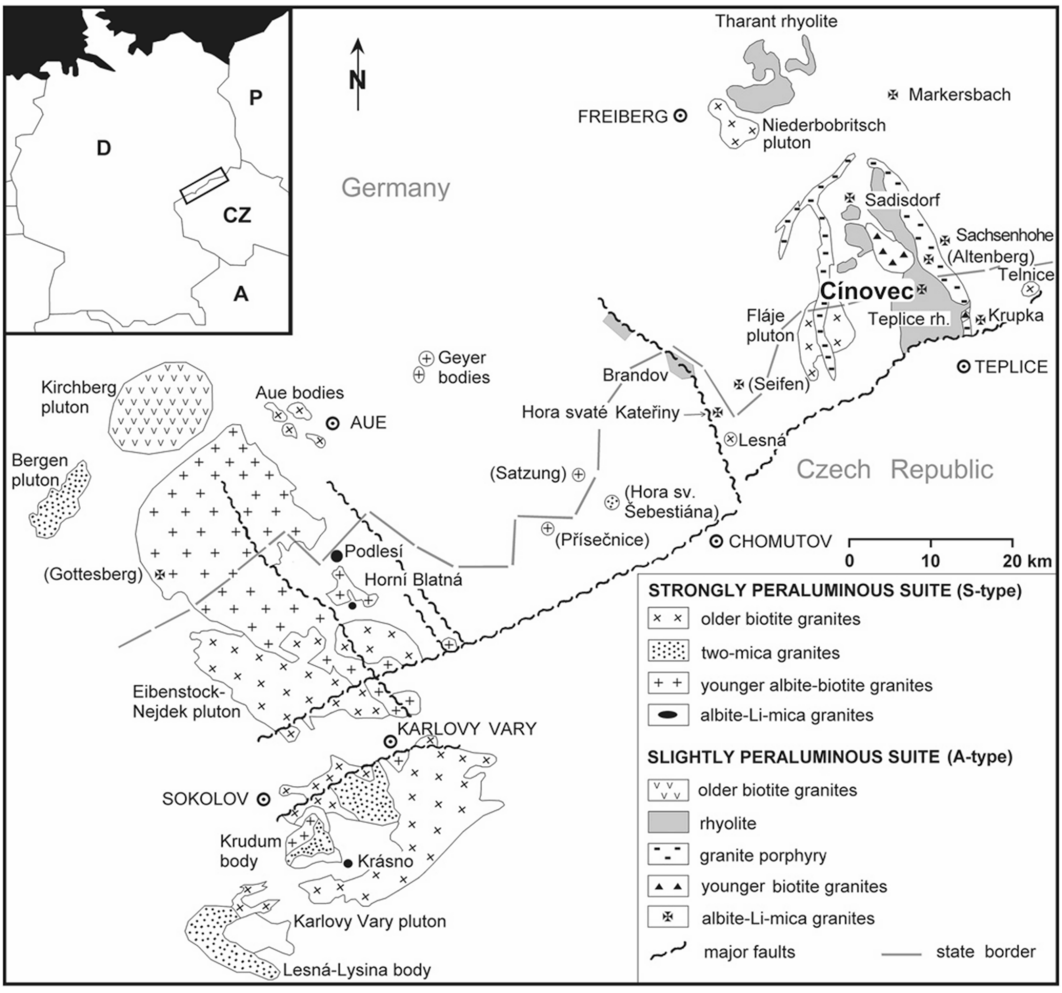


**Figure 1.** Geological map of Erzgebirge; small bodies of highly fractionated A-type granites (including Cínovec granite) are shown as Maltese cross symbols. Names of bodies without surface exposures are indicated in parentheses (after Breiter, 2012).

large hidden body with a small outcrop NW of Krupka. The equivalent in Saxony is the Shellerhau granite. All textural varieties contain drop-like quartz and orthoclase phenocrysts in a matrix consisting of quartz, oligoclase, perthitic orthoclase, and Li-bearing biotite. Fluorite and zircon are common accessories. (4) The relatively younger Cínovec granite forms an NW- to SE-elongated hidden ridge with a few small cupola- and stock-shaped outcrops. The main petrographic facies is characterized by medium-grained granite with phenocrysts of K-feldspar and drop-like quartz embedded in a quartz, albite, perthitic K-feldspar, and protolithionite matrix. Zircon, topaz, fluorite, cassiterite, monazite, thorite, xenotime, and rutile occur in accessory amounts. The upper level of the cupolas consists of medium-grained, non-porphyritic granite composed of quartz with albite inclusions, K-feldspar, albite, zinnwaldite, topaz, and fluorite. Cassiterite, scheelite, columbite, zircon, U-bearing pyrochlore, bastnäsite, and uraninite are the common accessories (Johan and Johan, 1994, 2005; Breiter and Škoda, 2012; Breiter et al., 2017a, c). The age of post-caldera rare-metal granites ($< 312$ Ma) remains controversial (Romer et al., 2007).

Small bodies (stocks and dikes) of similar Sn-, Nb-, and Ta-enriched granite were found at Seifen (Förster and Rhede, 2006) and Hora sv. Kateřiny (Breiter, 2008) in the central part of the Erzgebirge.

Hydrothermal activity following magmatic events produced numerous sulfide deposits of variable age, including sulfidic Pb–Zn–Ag deposits, five-element deposits (Ag–As–Bi–Co–Ni), and uranium vein deposits, as well as tin skarns and greisens. The metallogenesis of intrusion-hosted sulfidic mineralization in the Erzgebirge is mainly characterized by granite-related magmatic–hydrothermal systems. Proximal zones near intrusions feature oxide-dominated assemblages (e.g., cassiterite, wolframite), transitioning to distal base-metal sulfide mineralization (chalcopyrite, sphalerite, galena,

arsenopyrite) at greater distances from the granite contact (Leopardi et al., 2024; Weber et al., 2023). This zonation is primarily controlled by fluid–rock interaction along the hydrothermal pathway rather than temperature gradients, with sulfides forming late-stage veins and stockworks that overprint earlier oxide assemblages. Fluid inclusion data indicate that sulfide precipitation occurred under evolving physicochemical conditions, with fluid chemistry alterations and mixing (with meteoric or sedimentary fluids) driving metal deposition (Dolníček et al., 2012; Krejčí Kotlánová et al., 2024; Leopardi et al., 2024). The Sadisdorf deposit exemplifies this model, where chalcopyrite-rich and pyrite-rich sulfide subtypes occur in intermediate-to-distal settings, often crosscutting oxide veins. Whole-rock geochemistry further confirms that alkali depletion and greisen alteration (Li–Fe mica, topaz) precede sulfide mineralization, linking ore formation to the chemical evolution of fluids migrating away from the intrusion (Leopardi et al., 2024).

## 3 Cínovec deposit

The Cínovec deposit is located at the NW border of the Czech Republic in the Erzgebirge, in the eastern part of the Saxothuringian Zone of the Bohemian Massif. Part of the mineralization is located in Germany (Zinnwald deposit). Strongly fractionated A-type Cínovec granite of late Variscan age (age of surrounding rhyolite is 314–313 Ma, Tichomirowa et al., 2022) forms mostly buried mineralized cupola (of elliptical shape in N–S direction with 1.4 km in length and 0.3 km width). The granite is weakly peraluminous, enriched mainly in F, Li, Rb, Zr, Th, HREE, Sc, Sn, W, Nb, and Ta and poor in P, Ti, Mg, and Ca (Breiter, 2012). The cupola is composed of two main granite types – Li-, F-, Sn-, Nb-, Ta-, and Rb-enriched zinnwaldite granite (closer to the surface) and mostly barren biotite granite (in depth); volumetrically less important mica-free granite underlies the zinnwaldite granite (Fig. 2; Breiter et al. 2017b). In zinnwaldite granite, there are numerous greisen bodies and subhorizontal quartz–zinnwaldite veins. The cupola was examined to a depth of 1596 m by a structural drill hole CS-1 between 1961 and 1963, which intersected the pluton and provided important information about zoning and composition (Štemprok and Šulcek, 1969; Breiter et al., 2017a, b).

The Cínovec deposit is characterized by the vein-type and pervasive greisen-type Li–Sn–W mineralization. The vein-type mineralization is represented by flat quartz veins (commonly 20–50 cm thick) with zinnwaldite rims which contain cassiterite and wolframite and minor topaz, apatite, and scheelite; it was historically exploited mainly for cassiterite and, more recently, for wolframite. The greisen-type mineralization consists of irregular metasomatic bodies composed mainly of quartz and zinnwaldite (± topaz, fluorite, and remnants of feldspars). In this mass, fine-grained cassiterite and wolframite are scarcely disseminated together with columbite, ixiolite, scheelite, and other accessory minerals (Breiter et al., 2017c; Hreus et al., 2021).

Sulfide minerals at Cínovec have previously been studied mainly by Štemprok (1962, 1987) and Novák et al. (1991). Sulfide mineralization is characterized by complex paragenesis and a distinct spatial distribution within both gently and steeply dipping veins. Sulfides predominantly occur as irregular nests, impregnations, veinlets, or crystals in drusy cavities, with their quantitative contribution generally minor compared to the main gangue minerals. The most abundant sulfides identified at that time include arsenopyrite, molybdenite, stannite, galena, sphalerite, chalcopyrite, bornite, tennantite, chalcocite, pyrite, and covellite, often accompanied by native bismuth, bismuthinite, and rare roquesite. These minerals are typically younger than the principal gangue phases – quartz, zinnwaldite, topaz, and potassium feldspar – and are thus assigned to a distinct, late-stage sulfidic mineralization event. Textural relationships reveal that sulfides frequently form metasomatic replacements, veinlets, and breccia cements, with evidence of successive generations based on cross-cutting and overgrowth features. The genesis of these structures is interpreted in the context of solid-state diffusion and metasomatic processes, with the sulfidic stage further subdivided into pre- and post-baryte periods. Based on the production data from massive greisens in the southern part of the cupola between 1985 and 1990 (David, 1991), recovered sulfides accounted for approximately 13.9 g $t^{-1}$ of the Li–Sn–W ore material only.

## 4 Material and methods

Studied samples were mainly selected from drill cores produced as a part of the Cínovec project in the Czech part of the deposit (kindly provided by Geomet s.r.o.). All drill core samples are from the southern part of the Cínovec district from disseminated mineralization in massive greisens, where sulfides are generally more common than in the northern part (Fig. 2). Samples from the veins were obtained from the mineralogical collection of the National Museum, Prague; their exact position at the deposit is unknown as they were collected during mining activity in the Czech part of the deposit, i.e., likely from the vein system in the cupola center. From the collected samples, 15 polished thin sections and 14 polished mounts were prepared. A list of samples studied is provided in the Supplement (Table S1).

### 4.1 Electron microprobe analysis (EMPA)

The composition of sulfides was determined using two CAMECA SX100 electron probe microanalyzers (EPMA) at Masaryk University, Brno, and at the National Museum, Prague, in wavelength dispersion mode. For EMPA at Masaryk University, Brno, an accelerating voltage of 25 kV, a beam current of 20 nA, and a beam spot size of 2 µm were used. Standards used for the analysis were Cu on metallic

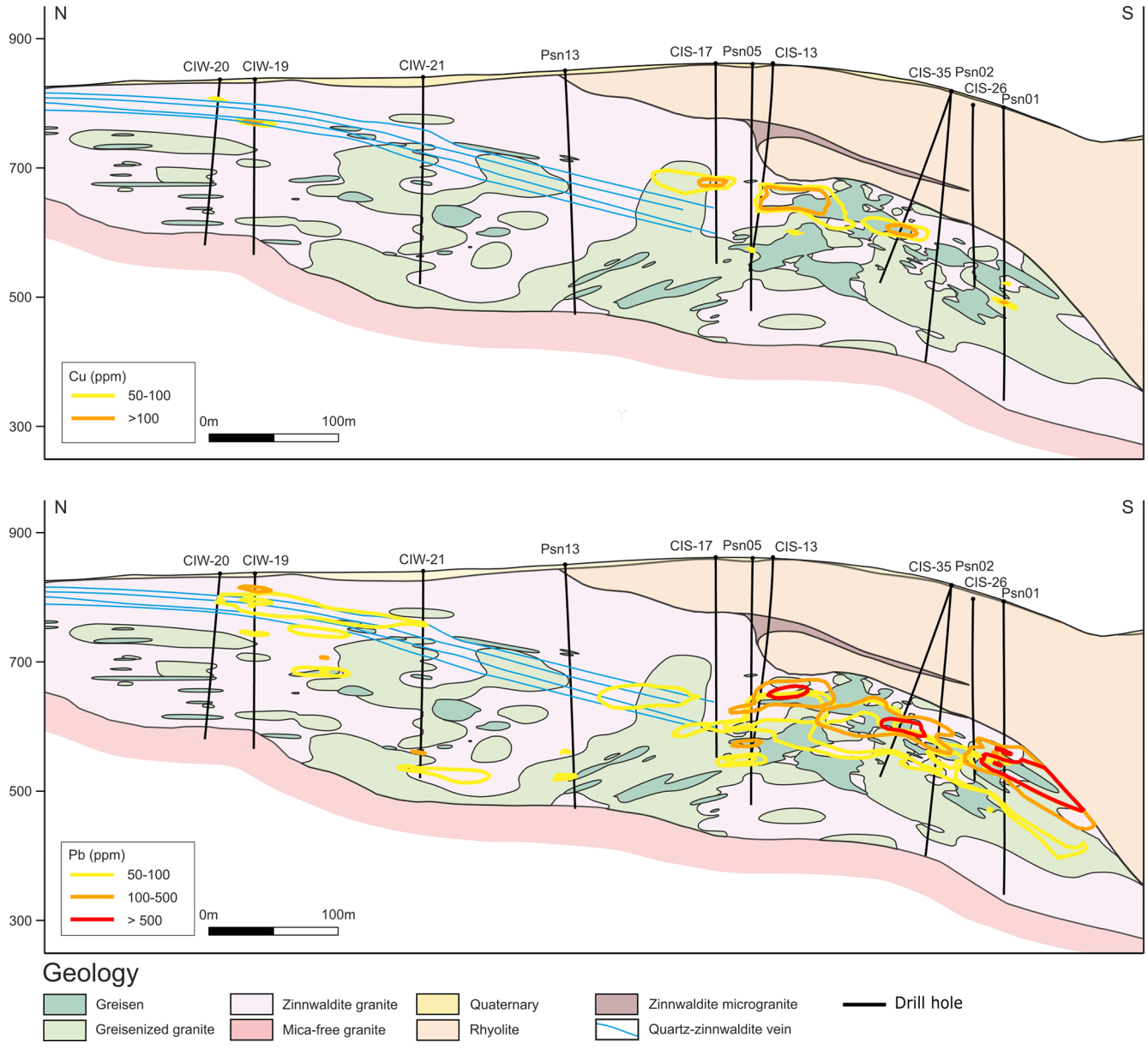


**Figure 2.**

Cu, Ni and As on pararammelsbergite, Co on metallic Co, Zn on $ZnS_2$, Fe on $FeS_2$, Se on PbSe, Ag on metallic Ag, S on chalcopyrite, Hg on HgTe, Sb on metallic Sb, Bi on Bi, and In on InAs. For all minerals, the correction procedure (X-PHI) described by Merlet (1994) was applied. For EMPA at the National Museum, Prague, an accelerating voltage of 25 kV, a beam current of 20 nA, and a beam spot size ca. 1 µm were used. Standards used were Sb on $Sb_2S_3$, Ag on metallic Ag, Pb on PbS, Te on PbTe, Cl on halite, Sn on Sn, Fe on pyrite, Ni on Ni, Co on metallic Co, Zn on ZnS, Cu and S on chalcopyrite, Hg on HgTe, Tl on Tl(Br,I), Bi on $Bi_2Se_3$, Cd on CdTe, Au on metallic Au, Cr on metallic Cr, As on NiAs, Se on PbSe, Ge on metallic Ge, In on InAs, Mn on metallic Mn, Ga on GaAs, K on sanidine, Ba on baryte, and P on fluorapatite. The PAP matrix correction was applied (Pouchou and Pichoir, 1985). Overlap corrections and peak calibrations were systematically incorporated. Compositional data from EMPA are provided in the Supplement (Tables S2–13).

## 4.2 Whole-rock analyses

The whole-rock abundances of both main and trace elements were acquired during the deposit study done by Geomet s.r.o. Parts (typically halves) of drill cores in intervals ranging from 20 to 200 cm were, after crushing and homogenization, analyzed in ALS Global employing the ME-4ACD81

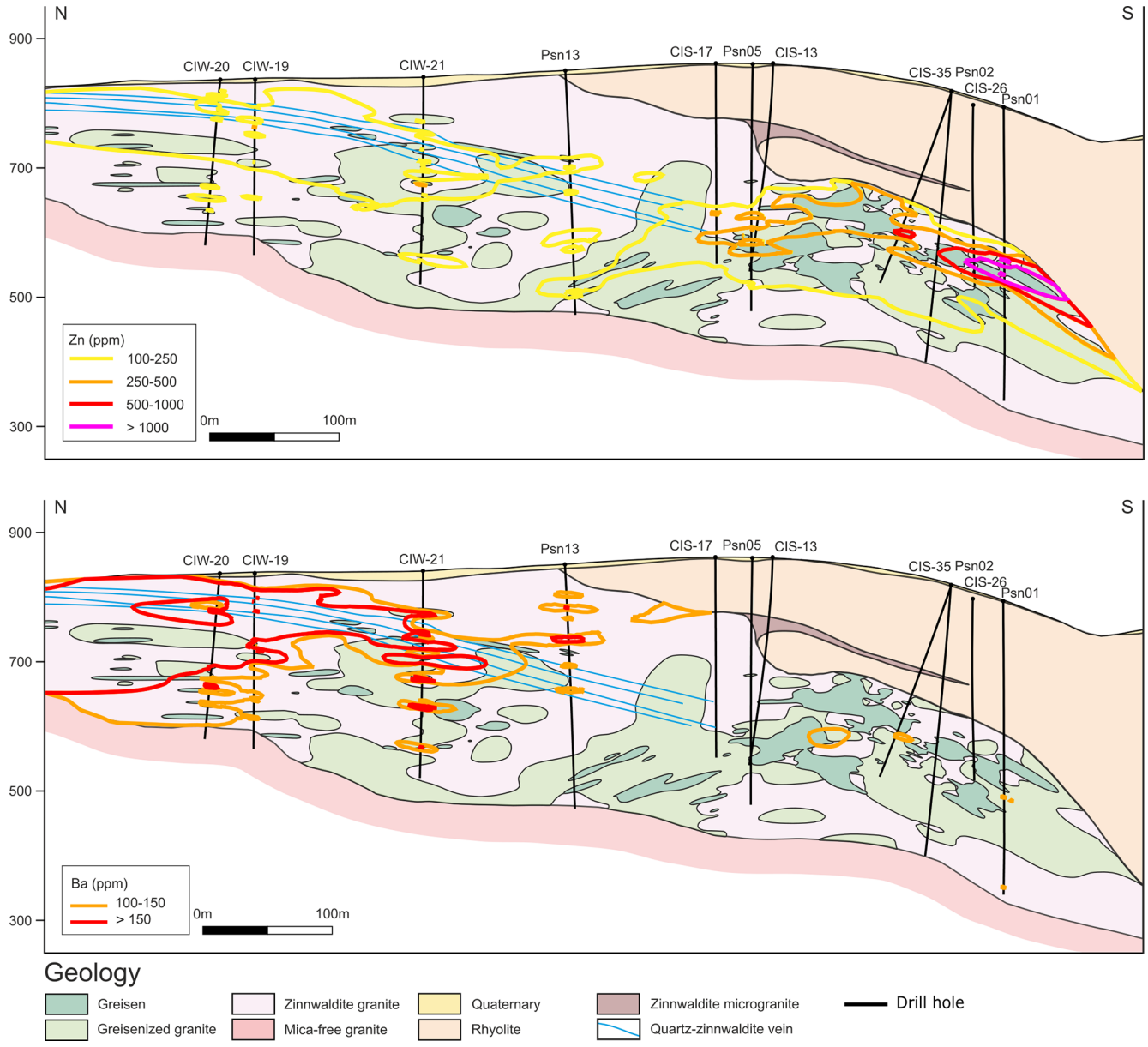


**Figure 2.** Cross-sections through the geological model of the Cínovec deposit, displaying the spatial distribution of Cu, Pb, Zn, and Ba. The deposit architecture features a cupola-shaped zinnwaldite granite intrusion overlain by the Teplice rhyolite (rock types after Breiter et al., 2017b). The Li–Sn–W mineralization is present in greisenized granite (pale green), greisen bodies (dark green), and quartz–zinnwaldite veins (blue).

(base metals by ICP-AES) and ME-MS81 (lithium borate fusion followed by ICP-MS) packages from the ALS Global Geochemistry Fee Schedules (https://www.alsglobal.com/en/Resources-and-downloads, last access: 7 May 2026).

### 4.3 Automated mineralogy (TIMA)

The Tescan integrated mineral analyzer (TIMA) solution in the R&D laboratory of TESCAN GROUP a.s., Brno, Czech Republic, was used to characterize selected thin sections and epoxy blocks in order to obtain the modal composition of the rocks, grain size distribution, and associations of the relevant ore minerals, bulk chemical composition, and elemental deportment and to understand the textures on a thin-section level. The machine combines signals from a BSE detector and up to four EDS detectors to distinguish individual phases and create mineral images, which are interpreted in dedicated software (see Hrstka et al., 2018). The following analytical conditions were used for acquisition: an accelerating voltage of 25 kV and probe current of 10 nA. Samples C1/205 and

P1/250 were analyzed using the "dot mapping" mode (see details in Hrstka et al., 2018), with a 1 µm BSE and 5 µm EDS grid; samples C73, C74, and C75 were analyzed with dot mapping, with a 2 µm BSE and 6 µm EDS grid; and samples C62–64, C65–67, C68, C69, C70, C71, C72, C76, and C77–78 were analyzed using Bright-phase search sections (Hrstka et al., 2018), with a 2 µm BSE grid and 2 µm EDS grid for phases with brightness above the 25 % BSE threshold and their immediate surrounding and a 6 µm EDS grid for phases with brightness below the 25 % BSE threshold. For all samples, SE and CL images were acquired simultaneously with BSE and EDS. The data were measured and processed in TIMA 2.12 software.

### 4.4 Raman spectrometry

Identification of some mineral species (pyrite, marcasite, enargite) was done using the Raman spectrometer Horiba Labram HR Evolution at the Department of Geological Sciences, Masaryk University, Brno. This dispersive, edge-filter-based system is equipped with an Olympus BX 41 optical microscope, a diffraction grating with 600 grooves per millimeter, and a Peltier-cooled, Si-based charge-coupled device (CCD) detector. The Raman signal was excited by a 633 nm laser. The nominal laser beam energy of 50 mW was attenuated to 5 or 12.5 mW using a neutral density filter to avoid the thermal damage of the analyzed area. The Raman signal was collected in the 100–900 $cm^{-1}$ range using a 600 gr $mm^{-1}$ grating and a 50× objective. The system was operated in confocal mode with a beam diameter of ∼ 1 µm. No visual damage to the analyzed surface was observed after the excitation. Raman-shift calibration was done using a silicon wafer. The wavenumber accuracy was ∼ 0.5 $cm^{-1}$, and the spectral resolution was ∼ 2 $cm^{-1}$.

## 5 Distribution of the sulfide mineralization at the Cínovec deposit

Based on the information from drill logs, the geochemical data on base metal distribution represent mainly the disseminated sulfide mineralization in massive greisens; horizontal veins were intersected relatively rarely (Fig. 2), and vertical veins were not encountered during vertical drilling. The dataset does not contain assays from the Teplice rhyolite as it does not contain significant Li mineralization and was therefore not analyzed. From the drill hole and geochemical data, it was possible to construct a 3D model and cross-sections showing the distribution of sulfide mineralization. The most significant geochemical indicators of mineralization are the contents of Zn, Pb, and Cu. The cross-section of the Cínovec deposit with the extent of sulfide mineralization is shown in Fig. 2.

The majority of sulfide mineralization is located in the southern part of the deposit in greisens and greisenized granites below the rhyolite contact (Fig. 2). Copper occurs at relatively lower concentrations in greisens in the upper part of the cupola, rarely exceeding 100 ppm. On the other hand, Pb demonstrates broader zones of enrichment, reaching over 500 ppm locally; high values are spatially clustered right below the rhyolite contact. Similar to lead, Zn is mainly concentrated below the rhyolite–greisenized granite contacts; Zn displays the highest concentration values exceeding 1000 ppm in a narrow zone (Fig. 2). In contrast to Cu, Pb, and Zn, high Ba contents are mainly located in the northern and northwestern parts of the deposit, while they are almost absent in the southern part (Fig. 2). Ba distribution is more dispersed, and values over 150 ppm are present mainly in zinnwaldite granite and greisenized granites.

The hydrothermal sulfide mineralization at the Cínovec deposit is later than the greisen and the hydrothermal quartz–zinnwaldite vein mineralizations (Štemprok 1987), but it may concentrate in zones of earlier tectonic predisposition, e.g., in quartz–zinnwaldite veins or surrounding greisens. Our samples are represented by three textural-paragenetic types: (a) prevailing flat-lying and less represented vertical quartz–zinnwaldite veins, (b) disseminated mineralization in massive greisen bodies and veinlets in granite or rhyolite, with rare (likely remobilized) sulfides observed in later (c) baryte–fluorite vein mineralization.

### 5.1 Quartz-zinnwaldite veins

Flat-lying quartz–zinnwaldite veins are identical in their mineralogical composition to steep veins (Štemprok, 1987) and most likely formed during the same genetic event; besides field observations (Štemprok, 1987), this is supported by the geochemical similarity of their quartz (Müller et al., 2018).

Sulfides occur in fractures (Fig. 3a, b) or in pockets (Fig. 3c), typically in centers of quartz–zinnwaldite veins; they form accumulations and irregular lenses of arsenopyrite, molybdenite, sphalerite, tennantite, galena, stannite, Cu sulfides, Bi minerals, pyrite, and opal (David, 1991). They either accompany the Li–Sn–W mineralization or the veins contain sulfide minerals only. The veins are characterized by the presence of several generations of coarsely crystalline quartz from the hydrothermal greisen stage preceding the sulfide mineralization and by the presence of fine-grained quartz on fractures filled with sulfides. In quartz–zinnwaldite veins, sulfide mineralization can form massive accumulations more than 10 cm large (Fig. 3).

### 5.2 Disseminated mineralization

Disseminated mineralization is volumetrically the most common type of sulfide mineralization at the deposit. It occurs in greisen and greisenized granites in the form of disseminated typically fine-grained subhedral grains to smaller sulfide aggregates. The main sulfide minerals encountered during past mining were galena and sphalerite, which accounted for

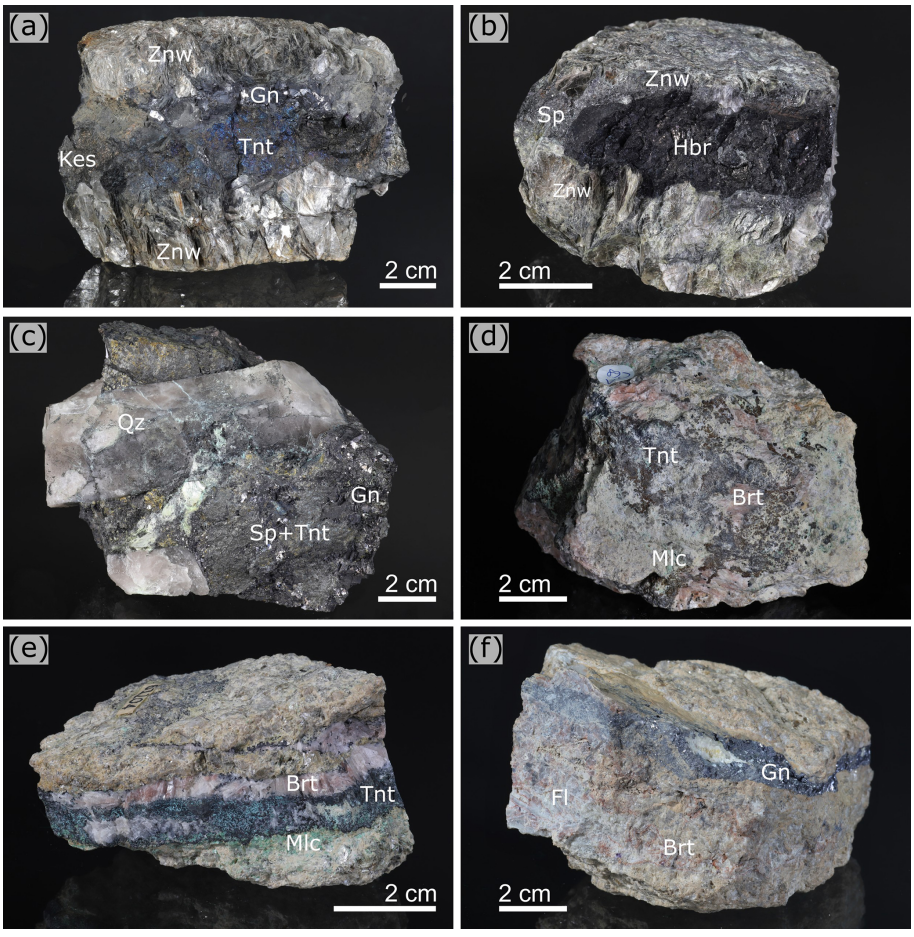


**Figure 3.** Representative samples of the studied vein sulfide mineralization. **(a)** Narrow quartz vein with zinnwaldite on its rims and massive késterite, galena, and tennantite in its center; **(b)** narrow quartz vein with zinnwaldite on its rims and a wolframite (hübnerite) rimmed with sphalerite and tennantite in its center; **(c)** center of a thick quartz vein with a massive galena, sphalerite, and tennantite ore filling a void around quartz crystal; **(d)** baryte vein with tennantite and malachite; **(e)** baryte vein with impregnations of tennantite and malachite from an altered zone in granite; and **(f)** late-stage vein with fluorite, baryte, and galena in altered granite. Mineral abbreviations (after Warr, 2021): Brt – baryte, Fl – fluorite, Gn – galena, Hbr – hübnerite; Kes – késterite, Mlc – malachite, Qz – quartz, Sp – sphalerite, Tnt – tennantite, and Znw – zinnwaldite. Samples C70 **(a)**, C74 **(b)**, C77 and C78 **(c)**, C68 **(d)**, C73 **(e)**, and C75 **(f)**.

80 wt %–85 wt % (galena) and 5 wt %–10 wt % (sphalerite) of sulfide concentrates (David, 1991). In contrast to the veins, copper minerals (tennantite, chalcopyrite) are rare. Interaction of the fluids producing disseminated sulfides with Sn,W mineralization was locally encountered as texturally distinct assemblages. Thick-tabular crystals of wolframite I are recrystallized to Mn-enriched rims and/or needle-like crystals of wolframite II that overgrow sphalerite (see Hreus et al., 2021) and can be covered by later galena and replaced by scheelite. Muscovitization of zinnwaldite and formation of secondary cavities filled with clay minerals are associated with the process.

### 5.3 Baryte–fluorite veins

Baryte–fluorite veins seem to be the youngest hydrothermal assemblage at the deposit, cutting granite, greisens, and the Teplice rhyolite. They are usually devoid of sulfides, but they frequently interfered with earlier mineralization, especially those with galena, and tennantite. The baryte veins therefore locally contain corroded/recrystallized tennantite, galena, and secondary Cu sulfides (covellite, digenite/roxbyite, anilite, djurleite), as well as malachite (Fig. 3d, e, f), minor Pb-rich baryte ("hokutolite"), and anglesite.

## 6 Sulfide mineralogy

The studied base-metal mineralization formed during multiple mineralization stages. They were distinguished based on the paragenetic position and textural features (especially fracturing, dissolution, replacement, recrystallization) of minerals present in individual assemblages. Their base-

metal sulfide minerals are reported in the temporal order of the individual mineralization stages.

### 6.1 Late greisen (K-feldspar) stage

#### 6.1.1 Molybdenite

Molybdenite occurs in association with Mo-rich scheelite I in quartz veins; hydrothermal breakdown of scheelite I (likely before and also during sulfide stages, Fig. 4a) results in formation of Mo-poor scheelite II and molybdenite in its vicinity, either on fissures in the altered scheelite I or in surrounding quartz.

#### 6.1.2 Arsenopyrite and safflorite

Arsenopyrite is the oldest sulfide, related to the end of the greisen stage (e.g., Štemprok, 1962, 1987); it occurs typically in quartz veins in assemblage with cassiterite, but it was also very rarely found in the disseminated mineralization where it forms inclusions in cassiterite or irregular grains in zinnwaldite (Fig. 4b, c). It is sometimes associated with later sphalerite and galena (Fig. 4b, c, e). Arsenopyrite is very close to the ideal formula (Table S2); it locally contains inclusions of Fe-rich safflorite with empirical formula $(Co_{0.56}Fe_{0.46}Ni_{0.02})(As_{1.86}S_{0.14})$ and minute euhedral cassiterite. The observed assemblage supports the earlier interpretation (David, 1991) that arsenopyrite and Co and Ni arsenides are the earliest phases of the sulfide mineralization directly associated with greisen-stage cassiterite.

### 6.2 Early sulfide stage (Cu, Sn, Zn, Fe)

#### 6.2.1 Stannite and kësterite

Stannite-group minerals (StnGM), kësterite (ideally $Cu_2ZnSnS_4$) and stannite (ideally $Cu_2FeSnS_4$), are less frequent accessory minerals related to the interaction of ore fluids with earlier Sn mineralization. Stannite with only a slight prevalence of Fe over Zn (in sample C70) and Fe-bearing kësterite (in samples C71 and C72) form large grains several millimeters in diameter enclosed within the silicate matrix or in later sulfides (Fig. 4d); they both seem to belong to the earliest sulfide generation, and, for simplicity, they are further called "*kësterite I*". Kësterite I (only in samples C71 and C72) reacted with sphalerite I, resulting in *kësterite II* and stannoidite I rims on their interface (Fig. 5); kësterite II forms slightly Fe-depleted rims of kësterite I grains on their contact with stannoidite (Fig. 4d). *Kësterite III* was found as minute (typically a few micrometers up to 20 µm large) inclusions in sphalerite I (Fig. 4e, f); rarely, overgrowth of kësterite III on euhedral sphalerite in a quartz vein pocket was observed (Fig. 4g). All kësterite generations and stannoidite were further replaced by tennantite, resulting in a fine-grained *kësterite IV* + tennantite ± cassiterite ± galena ± sphalerite II assemblage forming either veinlets cutting kësterite I and stannoidite I (Fig. 4g, i) or aggregates of sphalerite I with needle-forming cassiterite II (Fig. 4h).

StnGM show a wide range of Fe# = Fe / (Fe + Zn) (Table S3). The composition of kësterite I in sample C70 can be characterized as Zn-rich stannite at the borderline with Fe-rich kësterite (Fe# ∼ 0.49–0.53), whereas samples C71 and C72 contain Fe-bearing kësterite (Fe# ∼ 0.23–0.30). Interestingly, the latter composition has slightly elevated Cu and lower Sn contents (Fig. 6), suggesting transition towards theoretical Fe analogue of stannoidite. Kësterite II is compositionally very similar to kësterite I – it shows a minor depletion in Fe only (Fig. 5). On the other hand, kësterite III and IV have formulae close to the ideal kësterite end member (Fe# ∼ 0–0.05; Fig. 6b); due to a small grain size, analytical points in some of the kësterite III inclusions in sphalerite overlap with their host. The composition of stannite from sample C70 matches with the earlier published data (Štemprok, 1987) for stannite from Cínovec.

#### 6.2.2 Stannoidite

Stannoidite (ideally $Cu_8Fe_3Sn_2S_{12}$), another StnGM at the deposit, forms reaction rims around grains of Fe-rich kësterite I (samples C71 and C72) along their contact with sphalerite (*stannoidite I*); it locally encloses secondary cassiterite II (Fig. 4d). *Stannoidite II* forms small exsolved grains in sphalerite I. During the tennantite stage, *stannoidite III* also locally formed at the expense of needle-forming cassiterite II (Fig. 9a).

The composition of stannoidite is remarkable, characterized by its narrow range of Fe / (Fe+Zn) ∼ 0.65–0.74, regardless of its textural-paragenetic type and origin (Fig. 6). Stannoidite I is equivalent to the old names "*hexastannite*" and "*stannite I*" of Ramdohr (1980) and "*stannite I*" of Štemprok (1987), who described the same texture from the locality.

#### 6.2.3 Sphalerite

Sphalerite (ZnS) is the most common sulfide at the Cínovec deposit. The earliest *sphalerite I* corrodes grains of cassiterite I and kësterite I or cuts cassiterite I into veinlets and frequently encloses aggregates of needle-forming cassiterite II (Fig. 4a, d–f); sphalerite I typically reacted with kësterite I and formed a reaction rim of stannoidite I ± cassiterite II. Sphalerite I contains elevated contents of Cu, In, and Fe (Fig. 7a; Table S4). Sphalerite frequently contains numerous minute inclusions of kësterite and, in lesser amounts, also chalcopyrite (Fig. 4e), which likely represent intergrowths (Fig. 4e, i) or, rarely, exsolutions (Fig. 4f). Sphalerite II forms rims or recrystallized zones in sphalerite I, and it is depleted from Cu, In, and Fe after exsolution of kësterite II and chalcopyrite I (most likely in the galena and/or tennantite stages). Sphalerite III + tennantite cuts kësterite and stannoidite into

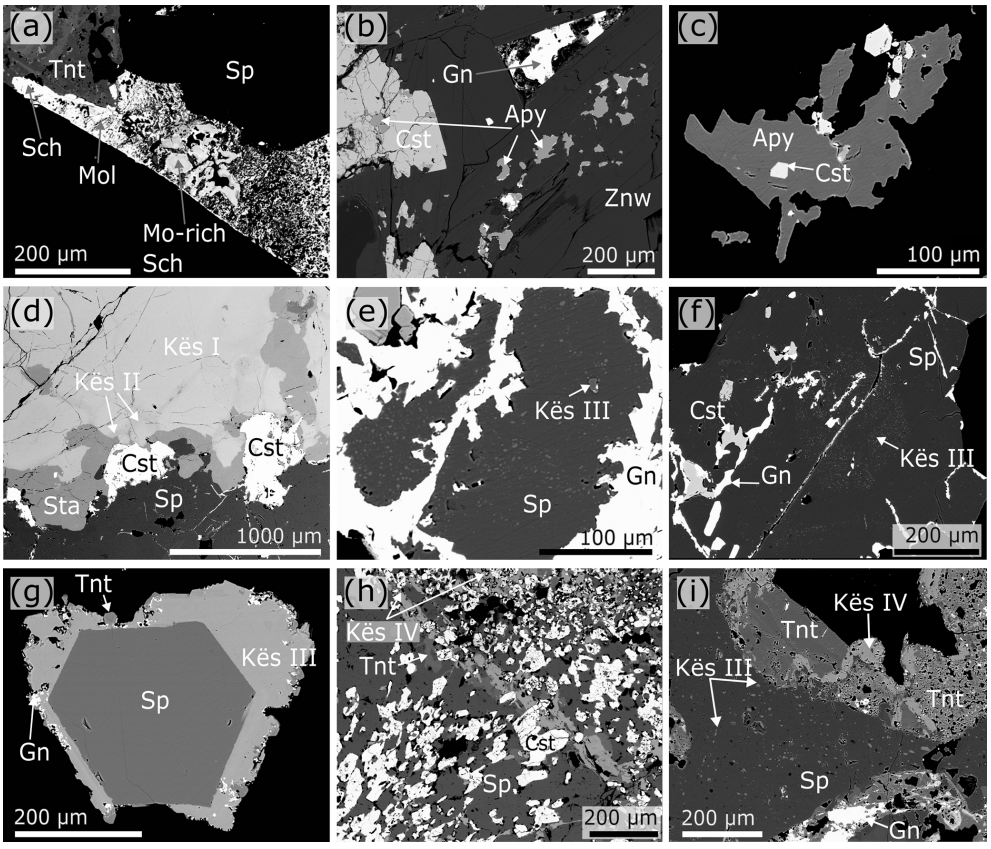


**Figure 4.** BSE images of early and intermediate sulfide mineralization assemblages from the Cínovec deposit. **(a)** Two types of scheelite with secondary molybdenite, enclosed in sphalerite at the contact with tennantite; **(b)** cassiterite I associated with arsenopyrite and galena; **(c)** arsenopyrite with inclusions of cassiterite; **(d)** large grain of këstérite I with stannoidite I and cassiterite II at its contact with sphalerite I; **(e)** corroded sphalerite I with këstérite inclusions, overgrown by galena; **(f)** sphalerite I with exsolved këstérite inclusions, with galena and cassiterite II on cracks; **(g)** euhedral sphalerite with këstérite rim corroded by galena and tennantite; **(h)** needle cassiterite in sphalerite matrix cut by këstérite and tennantite veinlets; and **(i)** sphalerite I with këstérite inclusions, replaced by këstérite and tennantite. Mineral abbreviations (after Warr, 2021): Apy – arsenopyrite, Ccp – chalcopyrite, Cst – cassiterite, Gn – galena, Kës – këstérite, Mol – molybdenite, Sch – scheelite, Sp – sphalerite, Sta – stannoidite, Tnt – tennantite, and Znw – zinnwaldite. Samples C74 **(a)**, CIS-1 191.05 **(b, c, e, f)**, C71 **(d)**, CIS1 205.5 **(g)**, C67 **(h)**, and CIS8 283.17 **(i)**.

thin veinlets (Fig. 5b). Sphalerite I is commonly enriched in indium (0.02–0.53 wt % In) and copper. Very low In concentrations are characteristic of sphalerite II and III; the positive correlation between In and Cu (Fig. 7) indicates the presence of a roquesite component in sphalerite. Contents of Fe are generally very low ($\leq 0.04$ apfu); only a few samples have up to 0.1 apfu Fe, which indicates an intermediate-to-low sulfidation state (near the pyrite–pyrrhotite boundary), which matches the typical conditions for Sn–Cu–Zn veins (Fontboté et al., 2017). Both in veins and in the disseminated mineralization, wolframite is partially recrystallized on its contact with sphalerite, resulting in the formation of Mn-enriched rims or needle-forming wolframite II overgrowths (for details, see Hreus et al., 2021).

### 6.3 Intermediate sulfide stage (Pb ± Bi, Ag)

#### Galena

Galena forms massive aggregates or euhedral crystals in the sulfidic assemblage; it typically cuts or rims earlier phases (këstérite I – stannoidite I, cassiterite I + II, sphalerite I) and may enclose aggregates of anhedral pyrite grains; very rarely, inclusions of cryolite were found in galena (sample C72). Galena is typically corroded during the tennantite stage, and there always seems to be some galena recrystallization, resulting in the presence of aikinite-group minerals and rare native Bi. Galena precedes crystallization of fluorite and baryte; they all fill pockets and impregnations in the late-stage assemblage of muscovite, K-feldspar (var. *adularia*), and fine-grained quartz.

Galena shows variable contents of Ag (up to 0.34 wt %) and Bi (up to 1.26 wt %) (Table S5). The Ag : Bi atomic ra-

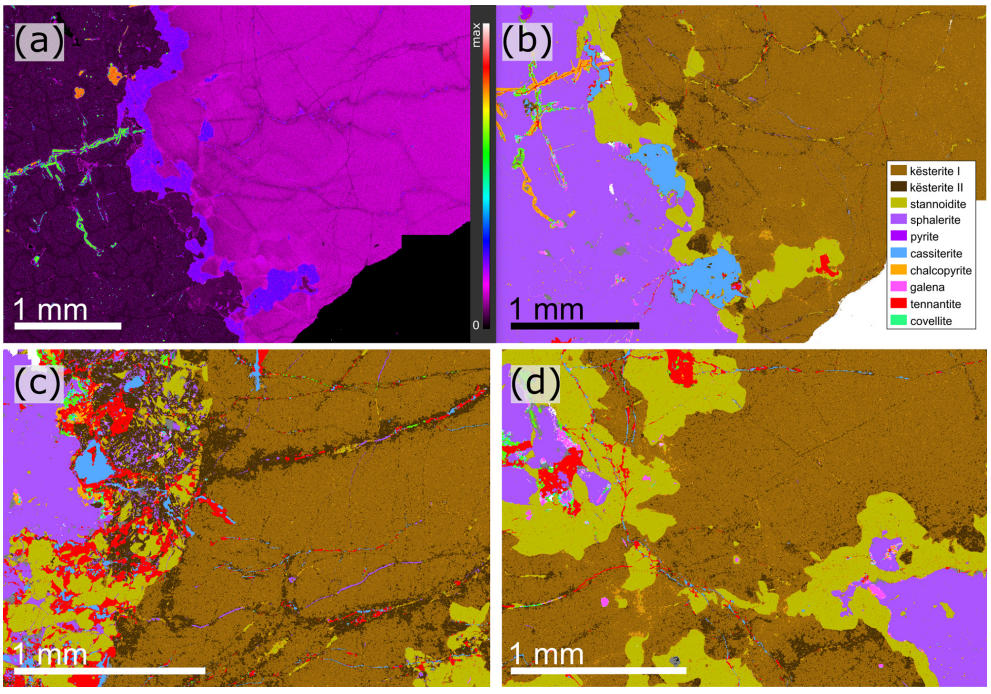


**Figure 5.** Images from TIMA showing replacement of kësterite I (Fe-rich kësterite) to stannoidite I and kësterite II at its contact with sphalerite. **(a)** Element map for Fe – note the Fe depletion in kësterite II in veinlets and at the rim of kësterite I; **(b)** mineral map of the same area as shown in **(a)**; **(c)** mineral map showing veinlets of sphalerite, tennantite, and cassiterite cutting kësterite I and replacing stannoidite; and **(d)** mineral map showing veinlets of tennantite and cassiterite cutting kësterite I and stannoidite. Sample C71.

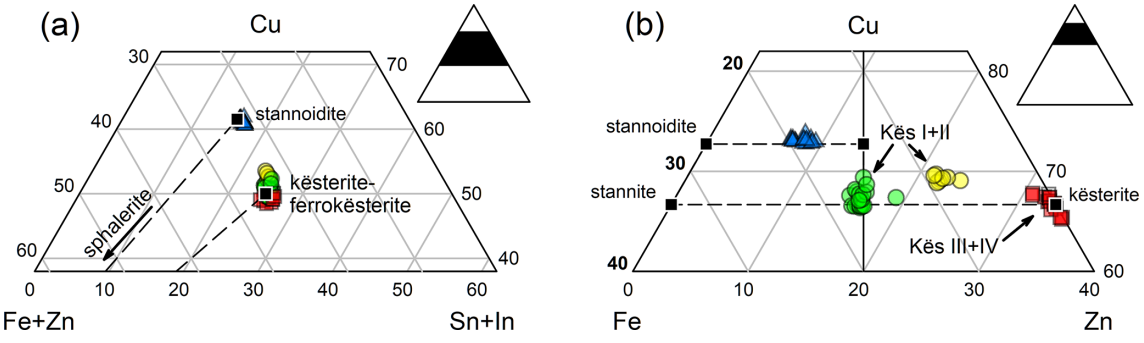


**Figure 6.** Ternary compositional diagrams (at. units) for kësterite–stannite and stannoidite. **(a)** Ratio of Sn + In vs. Cu vs. Fe + Zn. **(b)** Ratio of Zn vs. Cu vs. Fe. Green and yellow symbols – primary kësterite I with non-distinguished slightly Fe-depleted kësterite II (green symbols – sample C70; yellow symbols – samples C71, C72). Red symbols – kësterite III–IV. Blue symbols – stannoidite.

tio in galena ranges from 1 : 1 to 1 : 3, but there is no clear correlation between the two elements (Fig. 7b). Contents of Ag and Bi in galena are very variable, most likely due to its recrystallization during subsequent mineralization stages.

## 6.4 Late sulfide stage (As, Sb + Bi, Ag)

### 6.4.1 Pyrite and marcasite

In the samples studied, pyrite (locally intergrown with marcasite) rarely forms anhedral granular aggregates enclosed in galena (e.g., samples C66 and C7, C72; Fig. 8a, b) and fracture-filling impregnations enclosed in sphalerite close to or directly in chalcopyrite–tennantite veinlets (Fig. 8c, d). The identity of pyrite and marcasite (Table S6) was confirmed using Raman spectrometry.

### 6.4.2 Chalcopyrite

Together with tennantite, chalcopyrite is the major primary Cu mineral at the deposit. Chalcopyrite occurs in three generations: *chalcopyrite I* forms uncommon inclusions in sphalerite I; *chalcopyrite II* forms granular aggregates of rounded grains in galena, usually associated with pyrite, and tennan-

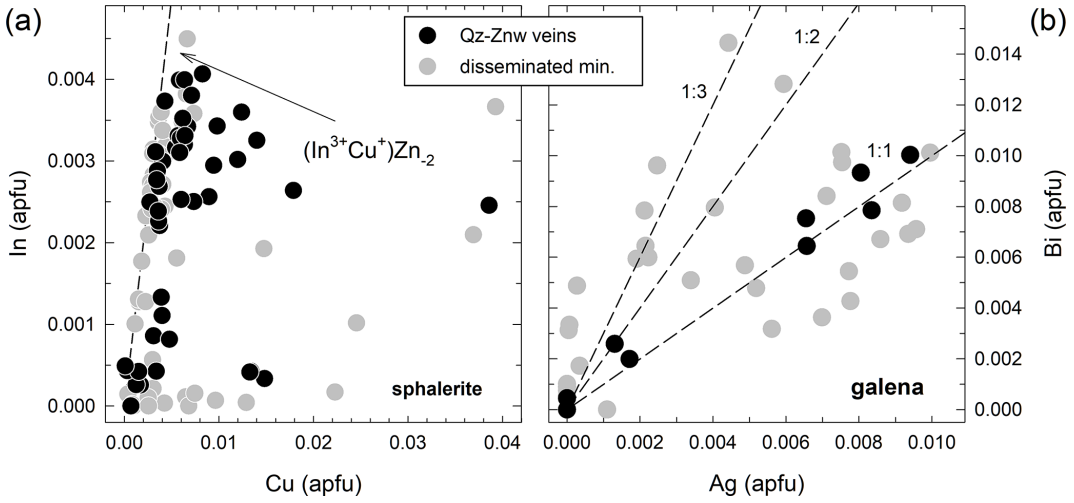


**Figure 7.** Contents of minor elements in sphalerite **(a)** and galena **(b)**.

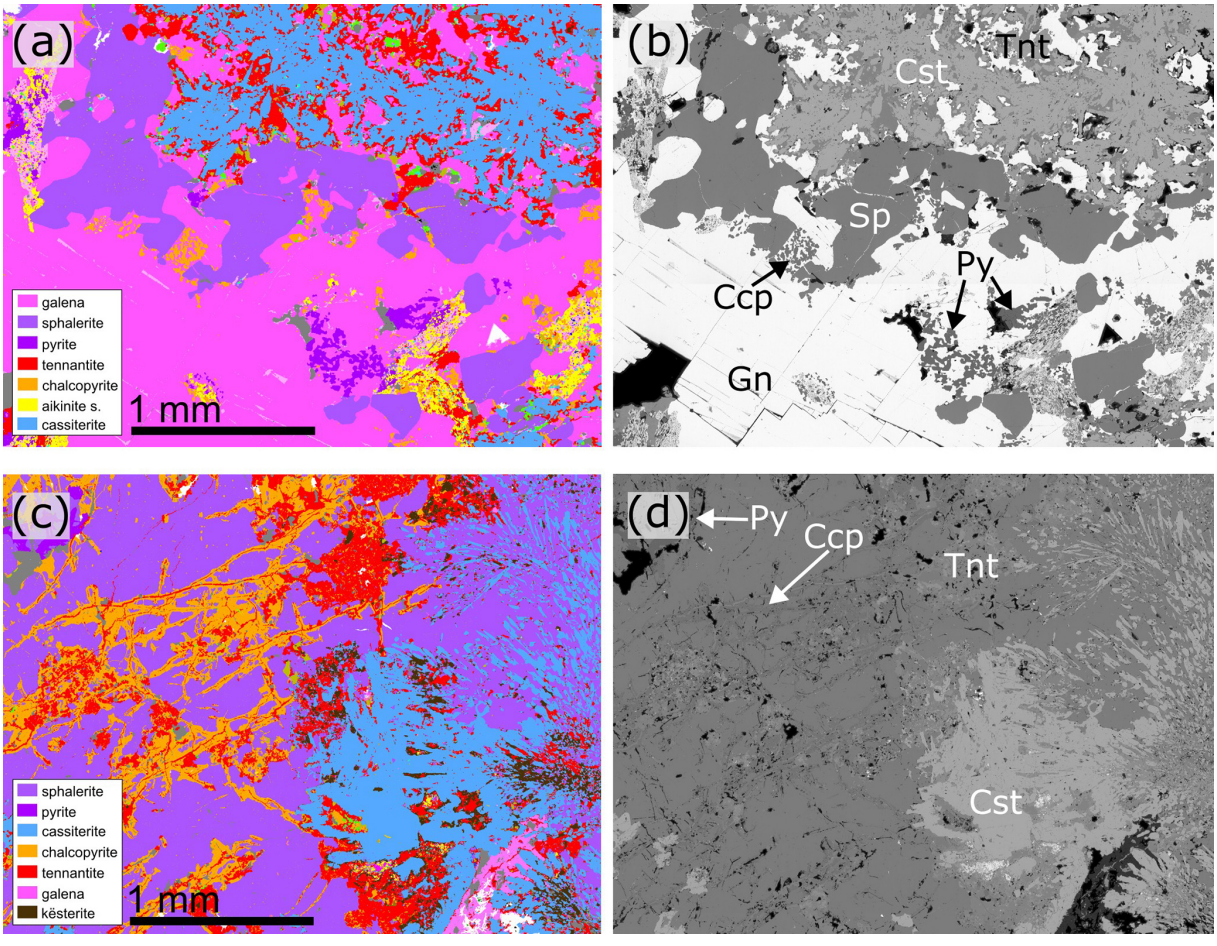


**Figure 8.** TIMA mineral maps and BSE images of textural features of sphalerite, pyrite, and chalcopyrite in assemblage with **(a, b)** and without **(c, d)** galena. **(a, b)** Granular aggregates of pyrite and chalcopyrite in galena near its boundary with tennantite + cassiterite assemblage; note the lobate boundaries of sphalerite enclosed in galena. **(c, d)** Fracture-filling assemblage of pyrite, chalcopyrite, and tennantite in sphalerite. Mineral abbreviations (after Warr, 2021): Ccp – chalcopyrite, Cst – cassiterite, Gn – galena, Py – pyrite, Sp – sphalerite, and Tnt – tennantite. Samples C66 **(a, b)** and C64 **(c, d)**.

tite or larger grains intergrown on their rims with aikinite–bismuthinite series minerals (Fig. 8a, b); and *chalcopyrite III* forms wide rims of tennantite veinlets cutting sphalerite (Fig. 8c, d) or small crystals on tennantite–tetrahedrite in pockets (Fig. 9b). All types of chalcopyrite display uniform chemical composition close to its ideal formula (Table S7). Locally elevated Zn contents in chalcopyrite I (up to 2.07 wt %) are most likely analytical overlaps from surrounding sphalerite.

#### 6.4.3 Tennantite–tetrahedrite

Tetrahedrite-group minerals occur in the disseminated mineralization and in massive aggregates up to several centimeters – exceptionally over 10 cm in size. They are frequently associated with sphalerite, chalcopyrite, or galena. From gangue minerals, they are typically associated with botryoidal quartz aggregates, fluorite, and baryte. Four paragenetic-compositional varieties can be distinguished.

*Tennantite I* replaces sphalerite in narrow zones or veinlets (Figs. 8c, 9c), and it is associated only with kësterite, stannoidite, and galena; its composition is almost exclusively close to the tennantite-(Zn) ideal end member.

*Tennantite II* forms zoned aggregates associated with galena and cassiterite II and minor stannoidite II/kësterite II. It has very low Sb, shows a stable Zn / (Fe + Zn) ratio from 0.08 to 0.17, and has a wide range of Bi / (As + Bi + Sb) from 0.04 to 0.40. The Bi content generally increases towards the border with corroded galena grains (Fig. 9d). The Bi-rich zones frequently enclose myrmekitic aggregates of Bi-rich minerals mostly of the aikinite–bismuthinite series (Fig. 9e). Locally, stolzite was found in tennantite near corroded galena grains (Fig. 9f).

*Tennantite III* forms zoned grains either disseminated in granite (samples Cis3 175.5 and PSn06 230.8), with a homogeneous composition and oscillatory-zoned, narrow Bi-enriched zones near their rims, or in a quartz vein (sample C74), where they form Sb-enriched zones in tennantite I or zoned aggregates and crystals in fluorite-filled pockets. It is represented mainly by As-bearing *tetrahedrite-(Zn)* and Sb,Fe-rich *tennantite-(Zn)*, with minor Sb-bearing *tennantite-(Fe)*. In the quartz vein, its composition gradually changes from tennantite-(Zn) to Sb,Fe-rich tennantite-(Zn) and Sb-bearing tennantite-(Fe).

*Tennantite IV* is associated with late-stage quartz and low-temperature Cu–S minerals (anilite, geerite, and spionkopite; Table S8, samples C62–C64). It can be porous sometimes. Its composition is characterized by higher $^{C}\mathrm{Cu}$ / (Zn + $^{C}\mathrm{Cu}$ + Fe) ratios.

Besides variations in the main species-defining elements at the C site (Cu, Zn, Fe) and D site (As, Sb, Bi) of the tetrahedrite-group mineral structure (Biagioni et al., 2020; Table S9), low to slightly elevated contents of Ag were detected (max 0.44 apfu, ∼ 3 wt % Ag), with most analyses below 0.1 apfu (avg. 0.05 apfu Ag). In Sb-bearing samples (tennantite III), Ag positively correlates with Sb, whereas in all other samples, Ag shows clear positive correlation only in Bi-rich tennantite II with > 1 apfu Bi (Fig. 10c, d). Elevated contents of Bi (up to 1.52 apfu) indicate the presence of up to 40 mol % of the annivite component (Sejkora et al., 2025).

#### 6.4.4 Cu sulfoarsenides (enargite, lautite)

Enargite, ideally $Cu_3AsS_4$, was rarely encountered as a corroded inclusion in tetrahedrite-(Zn) from a quartz–zinnwaldite vein (C73); in the same sample, lautite (ideally CuAsS) forms common inclusions in hydrothermally recrystallized tetrahedrite-(Zn) (note the darker and brighter shades of Tth in Fig. 9l), in the vicinity of secondary pores filled with digenite/roxbyite, djurleite, and pearceite (Fig. 9l). The composition of enargite is close to the ideal stoichiometry (Table S2), with minor amounts of Zn, Fe, Ag, and Pb (< 0.3 wt %). Similarly, lautite is close to the ideal formula (Table S2), with slightly elevated contents of Zn (0.29 wt %–0.42 wt %) and Ag (0.15 wt %–0.27 wt %). Enargite was distinguished from its tetragonal dimorph luzonite using Raman spectrometry.

#### 6.4.5 Cu–Ag–Bi–Pb sulfosalts (aikinite–bismuthinite series, emplectite, gustavite, berryite) and native Bi

Members of the aikinite–bismuthinite series are present both in quartz–zinnwaldite veins (bismuthinite, gladite, salzburgite, lindströmite, friedrichite, and aikinite were observed) and in the disseminated mineralization (bismuthinite, salzburgite, and aikinite). They frequently form nests or veinlets, intergrown with chalcopyrite and pyrite in galena, usually at the contact with tennantite (Fig. 9e); however, tennantite seems to corrode them (as well as the surrounding galena), resulting in Bi-rich tennantite zones (Fig. 9d, e). In the disseminated mineralization, bismuthinite was identified as the latest phase in the assemblage with galena and emplectite; aikinite and salzburgite were also rarely encountered (Table S10).

Minerals of the aikinite–bismuthinite series follow the bismuthinite–aikinite connecting line relatively closely, with minor deviations caused by a slight Cu excess (Fig. 11a). The members of the series were characterized using $n_{\mathrm{aik}}$ (Fig. 11b) calculated as $n_{\mathrm{aik}} = 25 \times (\mathrm{Pb} + \mathrm{Cu}) / 2$ according to Makovicky and Makovicky (1978).

*Emplectite* with a formula close to the ideal $CuBiS_2$ was encountered in the disseminated mineralization (Cis-9 284.15) in greisenized granite as narrow-zone rimming galena and as aggregates of acicular crystals enclosed in sericite and fluorite, overgrown by bismuthinite (Cis-8 282.55, greisen).

*Gustavite* was found as domains up to ∼ 30 µm large in a gustavite–berryite intergrowth enclosed in the center of concentrically zoned Bi-rich tennantite, in close association with

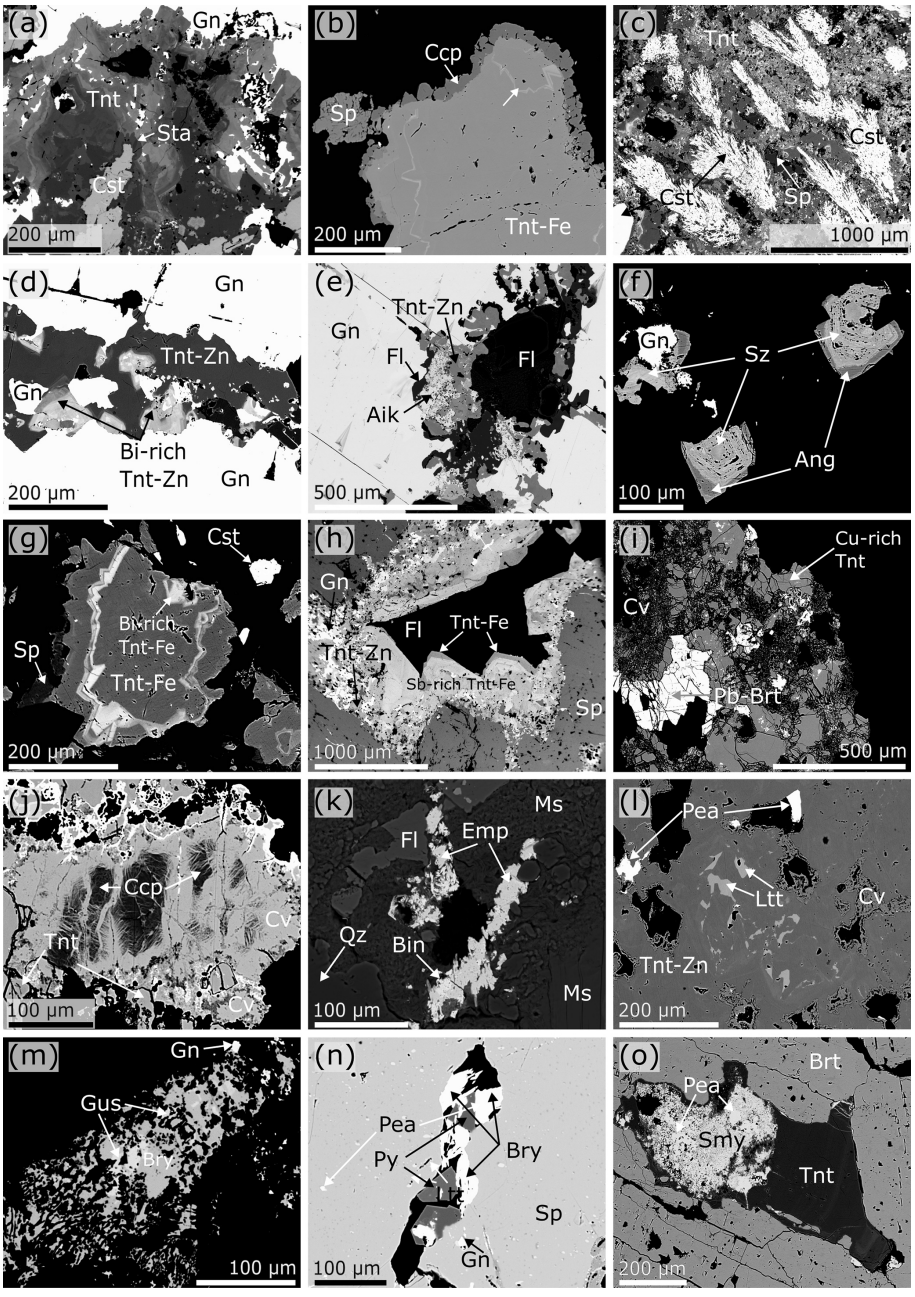


**Figure 9.** BSE images of late sulfide mineral assemblages from the Cínovec deposit. **(a)** Stannoidite III rim around cassiterite II, surrounded by zoned tennantite with inclusions of galena; **(b)** grain of tennantite-(Fe) overgrown by chalcopyrite and sphalerite, with arrowed bright zones of Bi,Sb-enriched tetrahedrite-(Zn); **(c)** needle-forming cassiterite II enclosed in tennantite and sphalerite; **(d)** galena with veinlet of tennantite-(Zn), with Bi-rich tennantite-(Zn) formed at the corrosive contact with galena; **(e)** fissure in galena with fluorite and aikinite corroded by Bi-rich tennantite-(Zn); **(f)** galena corroded by stolzite with anglesite rims; **(g)** tennantite-(Fe) with brighter zones enriched in Sb and Bi; **(h)** void in sphalerite rimmed with tennantite-(Zn), Sb-rich tennantite-(Fe), and tennantite-(Fe), filled by fluorite; **(i)** altered Cu-rich tennantite, covellite, and Pb-bearing baryte; **(j)** chalcopyrite and tennantite replaced by covellite; **(k)** fluorite, emplectite, and bismuthinite in muscovite–quartz matrix; **(l)** tennantite-(Zn) with lautite inclusions and alteration to covellite and pearceite; **(m)** intergrowth of berryite and gustavite; **(n)** berryite and pyrite on fissure in sphalerite; and **(o)** grain of tennantite enclosing pearceite and stromeyerite intergrowth, surrounded by later baryte. Mineral abbreviations (after Warr, 2021): Aik – aikinite, Apy – arsenopyrite, Bin – bismuthinite, Brt – baryte, Bry – berryite, Ccp – chalcopyrite, Cst – cassiterite, Fl – fluorite, Gn – galena, Gus – gustavite, Ltt – lautite, Ms – muscovite, Pea – pearceite, Py – pyrite, Qz – quartz, Smy – stromeyerite, Sp –sphalerite, Sz – stolzite, Tnt-Fe – tennantite-(Fe), and Ttn-Zn – tennantite-(Zn). Samples C66 **(a)**, CIS-3_175,5 **(b, g)**, C76 **(c, d)**, CIS-8_283,1 **(e, k)**, C78 **(f)**, C74 **(h)**, C62 **(i)**, C64 **(j)**, CIS-8 285.55 **(k)**, C73 **(l, o)**, and C67 **(m, n)**.

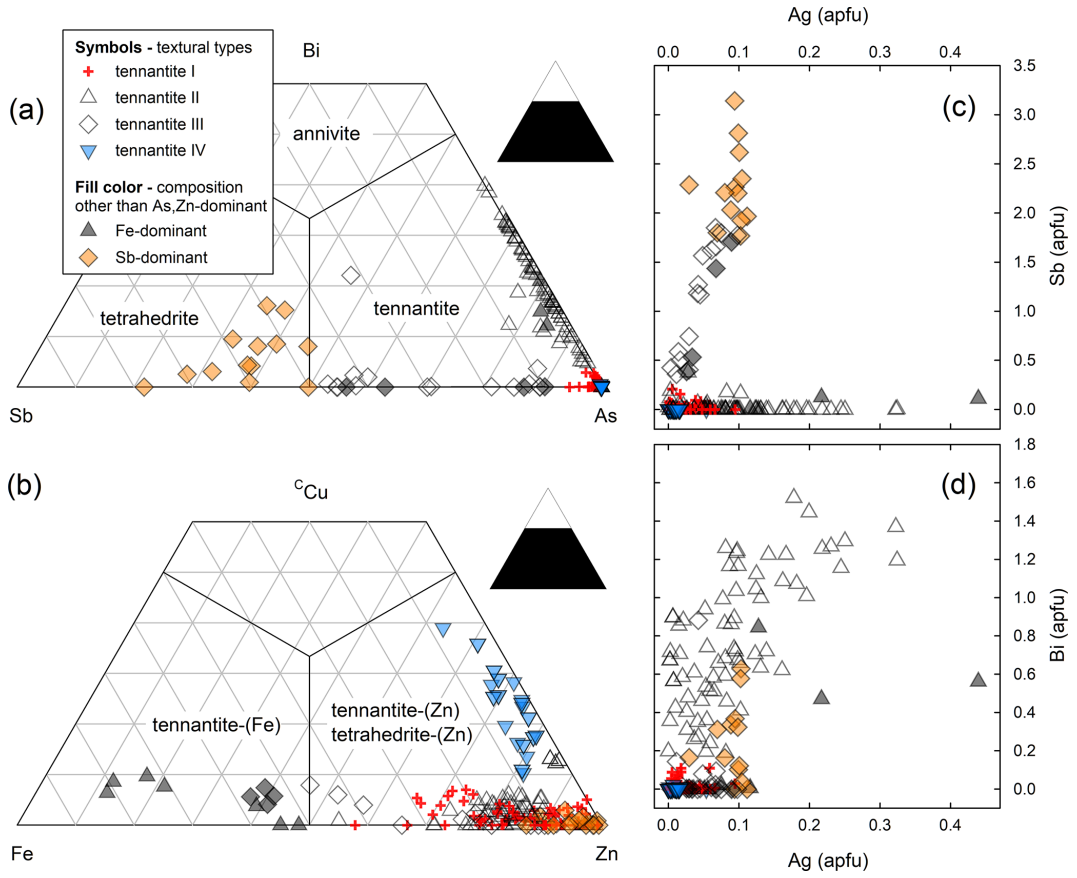


**Figure 10.** Compositional diagrams (at. units) for tetrahedrite-group minerals. **(a)** Classification ternary diagram of As–Bi–Sb based on the D-site occupancy, **(b)** classification ternary diagram of Zn–$^{C}$Cu–Fe based on the C-site occupancy, **(c)** diagram of Ag vs. Sb, and **(d)** diagram of Ag vs. Bi.

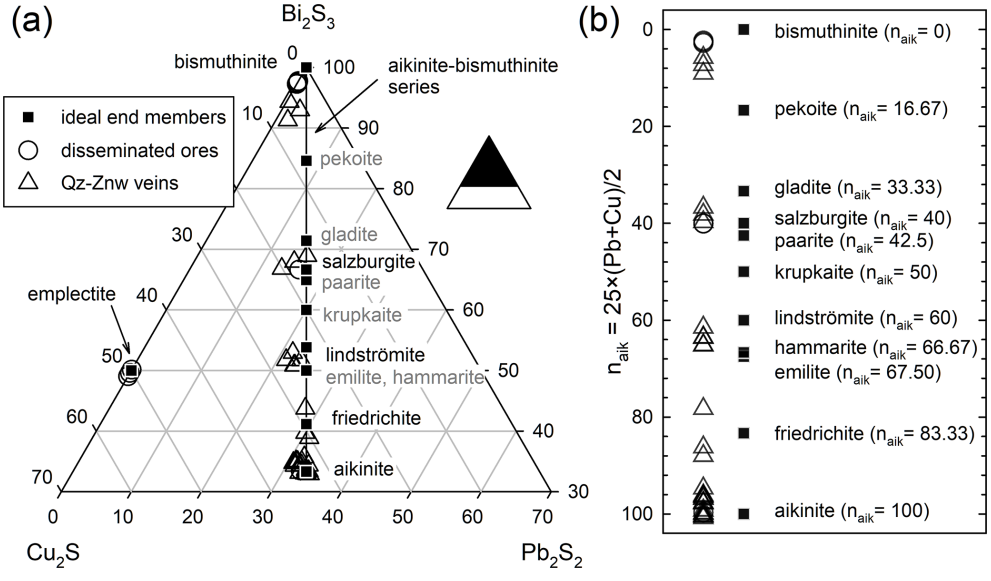


**Figure 11.** Diagrams showing compositional variation in the aikinite–bismuthinite series (at. units). **(a)** Ternary diagram showing molar ratios $Pb_2S_2$ vs. $Bi_2S_3$ vs. $Cu_2S$; **(b)** distribution of $n_{aik}$ for minerals of the aikinite–bismuthinite series.

skeletal cassiterite II (sample C67; Fig. 9m). Its composition shows slightly lower Bi (2.79–2.87 apfu) and slightly elevated Pb and Cu compared to the ideal $AgPbBi_3S_6$ stoichiometry; its $N = 4.26$–$4.56$ and $mol\%^{N}_{AgBi}L = 90$–$95$ (after Makovicky, 2019, Table S11) indicate that it represents a disordered transitional composition towards vikingite (Fig. 12) or can represent a disordered "Type 2 schirmerite" of Moëlo et al. (2008). Gustavite with similar disorder ($N \sim 4.39$–$4.51$) was described by Buzatu et al. (2015).

*Berryite* typically occurs as small aggregates up to 50 µm in association with pyrite enclosed in sphalerite (Fig. 9n) or in the form of isolated subhedral aggregates in tennantite. Strong variation in Cu (2.21–4.28 apfu) is less reflected in the contents of Ag (1.66–2.16 apfu), Pb (2.68–2.96 apfu), and Bi (6.10–6.92). Berryite also shows variable Zn contents in two samples; the textural position of the Zn-rich berryite grains in an open fissure in sphalerite and as an inclusion in tennantite suggests that the high Zn content may not necessarily be caused by overlaps of analytical spots with host minerals (Fig. 9n, Table S11).

*Native bismuth* was found as small inclusions in recrystallized galena.

#### 6.4.6 Cu sulfides from the Cu–S system

Copper sulfides ranging in stoichiometry between $Cu_{0.99}S$ and $Cu_{1.9}S$ form secondary zones around chalcopyrite and tennantite, commonly on their contacts with baryte/fluorite or as rims of small voids in tennantite (Fig. 9j, l). They sometimes occur together with agardite-(Y). In voids in tennantite, subhedral crystals of fluorite locally enclose the Cu-sulfide grains. The Cu / S ratio of the Cu sulfides indicates the presence of multiple species (Fig. 13; see, e.g., Sejkora et al., 2016), including covellite (Cu / S ∼ 0.99–1.04), geerite (Cu / S ∼ 1.53–1.63), anilite (Cu / S∼ 1.66–1.76), spionkopite (Cu / S ∼ 1.27), digenite/roxbyite (Cu / S∼ 1.8–1.82), and djurleite (Cu / S∼ 1.86–1.90). Previously reported chalcocite (e.g., Štemprok, 1987) was not encountered (Table S8).

#### 6.4.7 Cu–Ag(–As) sulfosalts (pearceite, cupropearceite, stromeyerite)

Minerals of the pearceite group and stromeyerite are locally found in assemblage with tennantite–tetrahedrite. In the disseminated sulfide mineralization (sample Cis-3 175.5), *Sb-rich pearceite* was rarely found as an inclusion in the chalcopyrite alteration rim around tetrahedrite. In quartz–zinnwaldite veins, *cupropearceite* with low Sb contents (Table S12) occurs with djurleite and digenite/roxbyite in pores and fractures of altered tetrahedrite-(Zn), sometimes enclosed in later baryte (Fig. 9l, o). It is locally associated with porous fine-grained *stromeyerite* with a composition close to ideal AgCuS (Table S13). Besides the large variation in Sb / (As + Sb), published compositions of As-dominant members (Bindi et al., 2007; Sejkora et al., 2026) show an extensive solid solution towards cupropearceite (Fig. 14). The cupropearceite from Cínovec is rather unique due to its near-ideal end member composition, comparable only to cupropearceite from Tsumeb (Bindi et al., 2015); slight Cu excess in part of the data (similar to the data of Bindi et al., 2015) cannot be readily attributed to an analytical point overlap.

## 7 Discussion

### 7.1 Crystal chemistry of sulfides and sulfosalts

Classification of Fe-rich members of the kësterite–stannite solid solution is rather complex. Kissin and Owens (1989) defined ferrokësterite as a low-temperature polymorph of stannite and Fe analogue of kësterite. Kissin (1989) noted a compositional Fe / Zn boundary between stannite and ferrokësterite at ca. $Fe_{0.75}Zn_{0.25}$ at 800 °C and showed the presence of minerals with a kësterite structure (either single or with stannite) in Fe-dominant synthetic systems down to 500 °C. From 700 to 600 °C, a single kësterite-structure phase was present from the $Fe_{0.5}Zn_{0.5}$ boundary to the $Zn_{100}$ composition; at 500 °C, a single phase was observed already from $Fe_{0.6}Zn_{0.4}$ (Kissin, 1989). On the other hand, Bonazzi et al. (2003) and Schorr et al. (2007) demonstrated the presence of a stannite structure ordering up to $Fe_{0.3}Zn_{0.7}$ on materials synthesized at 750 °C. The identification of ferrokësterite is rather problematic even from structural data (see, e.g., Bonnazzi et al., 2003), and there is a lack of experimental and especially structural works on transitional kësterite–stannite compositions that formed at temperatures lower than 600 °C; therefore, it is very problematic to classify them as either stannite or ferrokësterite based on their composition only. In this paper, we chose the conservative classification as stannite; however, further structural work would be necessary to clarify the mineral structural order and classification. Similar stannite and kësterite occurrences in the Erzgebirge include Vernéřov (Breiter et al., 2009b), where stannite (0.65–0.85 apfu Fe, 0.2–0.4 apfu Zn) replaces cassiterite and locally contains exsolution lamellae of kësterite (ca. 0.65 apfu Zn).

The stable Fe / Zn ratio in stannoidite from different mineralization stages indicates that it might be constrained by its crystal structure stability. Yamanaka and Kato (1976) showed that two out of three Fe atoms in the stannoidite structure are oxidized to $Fe^{3+}$, and the crystal–chemical formula of stannoidite is therefore $Cu^{1+}Fe^{3+}_2Fe^{2+}Sn^{4+}_2S^{2-}_{12}$; as Zn substitutes for $Fe^{2+}$ only, the ratio Fe / (Fe + Zn) = 0.66 represents the structurally constrained limit for Fe–Zn exchange. The Fe / (Fe + Zn) range of 0.65–0.74 for the Cínovec stannoidite agrees with its formation in Zn-saturated local systems involving sphalerite or tennantite-(Zn). The texture where stannoidite I forms rims around corroded Fe-bearing kësterite (Fig. 5) indicates kësterite replacement; the process can be

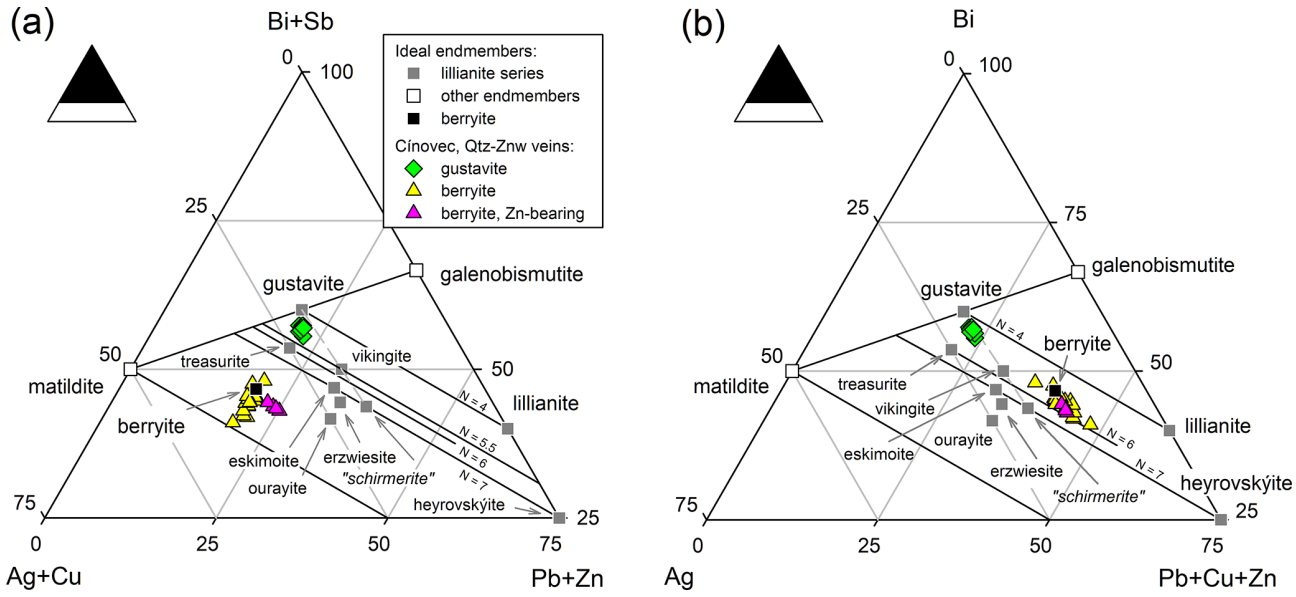


**Figure 12.** Ternary diagrams showing compositional variation in gustavite and berryite (at. units).

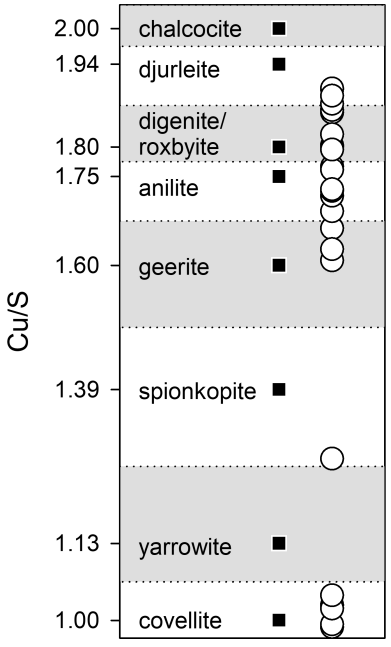


**Figure 13.** Diagram showing atomic Cu / S ratios (at. units) for sulfides from the Cu–S system. Ideal end members are plotted as squares, and data from Cínovec are plotted as circles. Data ranges for chalcocite and covellite and mineral element ratios are from Sejkora et al. (2016).

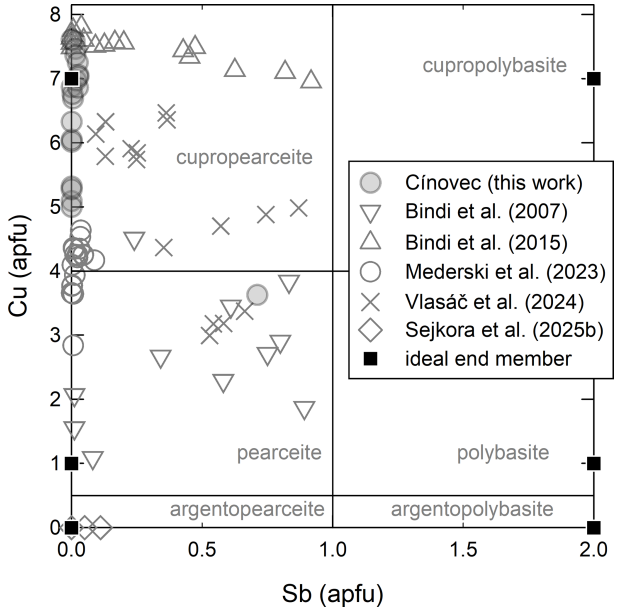


**Figure 14.** Compositional diagram for cupropearcerite and pearcerite from Cínovec compared to published data for As-dominant members of the pearcerite–polybasite group (data from Bindi et al., 2007, 2015; Mederski et al., 2023; Vlasáč et al., 2024; Sejkora et al., 2026). Note: the classification borderlines are valid for Au-, Te-, and Se-free pearceite- and polybasite-group mineral compositions only.

represented by the following reactions:

$$4Cu_2^+(Fe^{2+}{}_{0.3}Zn_{0.7})SnS_4 + 0.8FeS + 2O_2$$
$$= Cu_8^+(Fe_2^{3+}Zn)Sn_2S_{12} + 1.8ZnS + 3S + 2SnO_2$$
$$4Cu_2^+(Fe_{0.3}^{2+}Zn_{0.7})SnS_4 + 0.8FeS + 4H_2O$$
$$= Cu_8^+(Fe_2^{3+}Zn)Sn_2S_{12} + 1.8ZnS + 3H_2S + H_2 + 2SnO_2.$$

A change in redox conditions took place with an influx of hydrothermal solutions producing sphalerite. FeS can be sourced from $FeS \leftrightarrow ZnS$ exchange that depletes kësterite

I from iron, resulting in kësterite II (Fe-depleted rims in Fig. 5a). The same texture was also described as a reaction rim by Ramdohr (1980; see his Fig. 107).

Tetrahedrite-group minerals (Biagioni et al., 2020) from the Cínovec deposit are the most important carriers of As within the sulfide paragenesis. In most of the samples analyzed, tennantite-(Zn) is a dominant phase of this group. Tetrahedrite-group minerals from the deposit frequently show elevated to high contents of Bi (up to 1.52 apfu Bi). Much higher Bi contents (locally up to 2.65 apfu) were reported by Gołębiowska et al. (2012) from Rędziny, Poland, and by Sejkora et al. (2025), who defined the first Bi-dominant member of the tetrahedrite group, annivite-(Zn). Other occurrences of the Bi-dominant analogue of tennantite and tetrahedrite are reported, e.g., by Bortnikov et al. (1979), Kieft and Eriksson (1984), Spiridonov et al. (1986), Velebil and Sejkora (2018), and Dolníček et al. (2024). The tennantite–tetrahedrite from Cínovec is locally enriched in Ag (e.g., David, 1991), which correlates positively with Bi in Bi-rich tennantite II (at Bi $>$ 1 apfu only) and Sb in tennantite III (Fig. 10c, d). Similar Bi-rich compositions are known from elsewhere in the Erzgebirge (e.g., Niederschlema-Alberoda and Jáchymov; Förster et al., 2004; Velebil and Sejkora, 2018) and Variscan orogene (e.g., central Schwarzwald, Staude et al., 2010) and are distinctly different from the Freiberg district (Burisch et al., 2019).

The chemistry of berryite from the Cínovec deposit shows significant variability (Fig. 12). Compared to the ideal formula $Cu_3Ag_2Pb_3Bi_7S_{16}$, it has elevated contents of Cu and in two samples also Zn. The excess of Cu has previously been described by several authors (e.g., Lowry et al., 1994; Cook, 1998; Topa et al., 2006; Sejkora et al., 2021). Variability of berryite chemistry within the deposit covers the variability of previously published berryite analyses from other localities around the world. A second occurrence from the Erzgebirge at Hřebečná (Sejkora et al., 2021) shows smaller ranges in Cu, Pb, and Bi concentrations and minor contents of Se.

The chemical composition of aikinite–bismuthinite series minerals shows wide variation. At the deposit, bismuthinite ($n_{aik}$ 2.55–9.08), gladite ($n_{aik}$ 36.72–38.16), salzburgite ($n_{aik}$ 39.73–40.04), lindströmite ($n_{aik}$ 61.49–65.18), friedrichite (78.27), and aikinite (86.22–100.82) have been distinguished. In several cases, aikinite with $n_{aik}$ over 100 was identified; it could be caused by other substitutions or possibly by the presence of a vacancy. Such a wide compositional variation within the aikinite–bismuthinite series within one locality is not common; it was known from the metamorphosed scheelite deposit in Felbertal, Austria (Topa et al., 2002), similarly also in the Gemerská Poloma tin deposit and in the associated hydrothermal veins (Števko and Sejkora, 2021; Kondela et al., 2025). The common feature of all the localities is a multi-stage hydrothermal overprint of the previous lithology.

### 7.2 Paragenetic relationships among mineralizations at the deposit

Besides early magmatic/metasomatic assemblages (Breiter et al., 2017b, c), the paragenetic sequence at the Cínovec/Zinnwald deposit (Fig. 15) reveals five distinct late metasomatic and hydrothermal mineralization stages, demonstrating the complex evolution of the deposit; their distribution generally corresponds to variance of Zn, Pb, Cu, and Ba within the deposit (Fig. 2). The earliest metasomatic (greisenization) stage is characterized by oxide–silicate assemblages (Johan and Johan, 1994, 2005; Breiter et al., 2017c; Hreus et al., 2021), with quartz and zinnwaldite formation in veins and granites, associated with, e.g., topaz, wolframite, and fluorite. It is important to note the positive correlation of Zn with Li (Fig. 2), which indicates that a large portion of Zn is contained in zinnwaldite due to $ZnFe_{-1}$ exchange (up to $\sim$ 1100 ppm Zn; Breiter et al., 2023, unpublished data of authors). The first sulfides are related to the subsequent potassic stage. It is marked by feldspathization, muscovitization (Breiter et al., 2017a), and the formation of cassiterite I, Mo-rich scheelite I, and likely also arsenopyrite and molybdenite, although the formation of the latter during alteration of scheelite I seems more likely. The early sulfide stage begins by the formation of early kësterite I (Zn-rich stannite or Fe-bearing kësterite), followed by its reaction with sphalerite, resulting in the stannoidite, kësterite II, and cassiterite II assemblage. The intermediate sulfide stage with galena introduced significant Ag and Bi contents into the system. The late sulfide stage is characterized by the introduction of As, Sb, and further Cu and likely Fe, resulting in common tennantite–tetrahedrite minerals, chalcopyrite, and remobilization of elements such as Fe + In from sphalerite and Bi+Ag from galena (producing aikinite–bismuthinite series, gustavite, berryite, emplectite). Native bismuth found locally in the studied samples but widespread at the deposit must have formed below 271 °C (melting temperature of Bi). Its position towards other minerals is unclear due to its scarcity.

The latest fluorite–baryte stage represents the waning hydrothermal system, with dominant baryte, minor fluorite, and (likely remobilized?) galena or tennantite. The occurrence of enargite in tennantite cut by the fluorite–baryte vein (sample C73) indicates temperatures above $\sim$ 280–300 °C (Pósfai and Buseck, 1998); however, enargite likely represents the tennantite (or galena) stage rather than the baryte–fluorite overprint. The low-temperature alteration of tennantite produced both sulfides (Cu sulfides ranging from covellite to djurleite, cupropearceite, etc.) and oxygen-bearing (e.g., malachite, anglesite, mimetite, agardite-(Y), chrysocolla) phases. Stromeyerite represents the lowest-temperature assemblages below 93 °C (Skinner, 1966). The alteration is clearly (at least in the studied samples) related to the fluorite–baryte stage – Cu sulfides in tennantite voids are sometimes overgrown by fluorite and baryte, which are later followed by Cu arsenates (sample C73). Alternatively, Cu sulfides

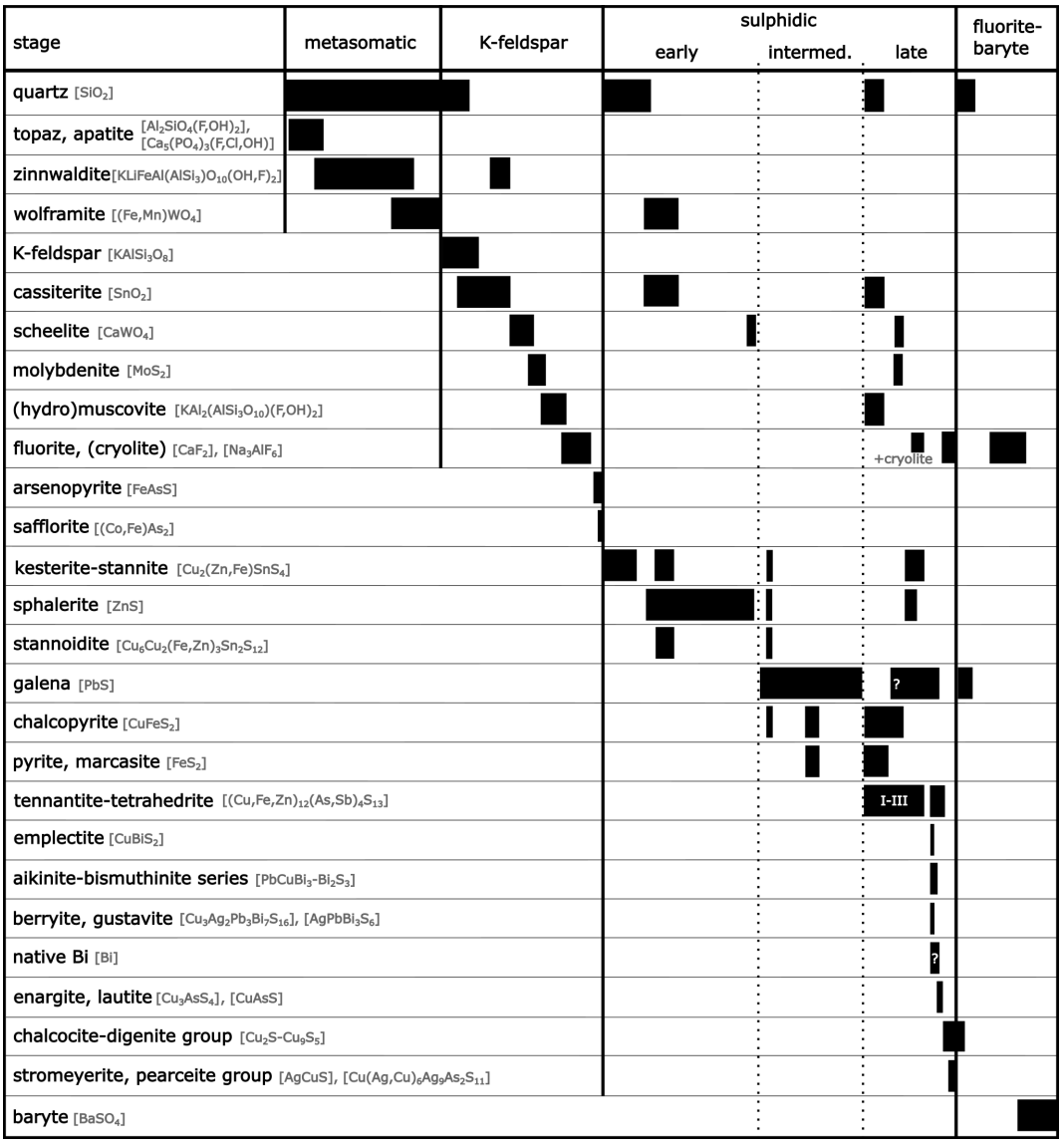


**Figure 15.** The paragenetic sequence of the main hydrothermal gangue and ore minerals at the Cínovec/Zinnwald deposit (modified and updated from David, 1991). Ideal formulae of minerals are shown in square brackets.

(covellite and djurleite) associated with mimetite occur in baryte voids, followed by calcite, muscovite, and kaolinite (sample C69). The textures suggest that the fluorite–baryte stage either followed after or, more likely, caused partial low-temperature overprint of the earlier sulfide assemblages.

Rare grains of cryolite matching the ideal formula $Na_3AlF_6$ were found as inclusions in low-Fe,Cu sphalerite and in galena, in both cases in the vicinity of tennantite and fluorite veinlets (samples C71 and C74). We assume that cryolite represents a rare product of albite and/or topaz reaction with remobilized fluorine-rich fluids.

David (1991) and Štemprok (1987) placed the tennantite stage after the fluorite–baryte stage. However, the textural-paragenetic features observed in our samples clearly show that tennantite precedes baryte formation. Fluorite occurs in several stages, including the end of the tennantite crystallization, which locally forms voids filled with fluorite. We assume that the earlier studies had to work with a limited number of samples where the two mineralizations intersect.

This sequence documents the evolving conditions from high-temperature (> 400 °C) magmatic–hydrothermal fluids to cooler (< 200 °C) late-stage fluids. A similar paragenetic sequence was encountered in the Krupka district located 6.5 km SE, also sourced from the Cínovec granite (e.g., Žák, 1966; Sejkora and Breiter, 1999), and is very similar for the whole eastern part of the Erzgebirge (e.g., Sadisdorf; Leopardi et al., 2024). The mineralization can be divided into two basic types – metasomatic bodies (greisens and "zwitters")

and ore veins, where sulfide and fluorite–carbonate stages can be distinguished (Žák, 1966; Sejkora and Breiter, 1999; Krejčí Kotlánová et al., 2024).

### 7.3 Position of Cínovec in the context of sulfidic mineralization in the SE Erzgebirge

The NW–SE structural trend in the Teplice caldera related to intrusion of A-type granites (Breiter et al., 2017b) plays a fundamental role in controlling the spatial distribution of Sn–W–Li mineralization, as evidenced by numerous deposits on both the Czech and the German sides of the metallogenic province. Key examples include the Sadisdorf vein-type mineralization, the Krupka vein-type and greisen deposits, and the Cínovec/Zinnwald greisen system.

The relationship between Pb–Zn mineralization (galena, sphalerite) and greisen–vein systems can sometimes be characterized by spatial and temporal zonation linked to magmatic–hydrothermal fluid evolution. Greisen alteration driven by high-temperature (> 400 °C) fluids exsolved during late-stage granite crystallization typically hosts proximal Sn–W mineralization (e.g., cassiterite, wolframite) within or near granitic intrusions (Leopardi et al., 2024; Korges et al., 2018). As later fluids migrate through the intrusion fracture system outward, cooling (250–400 °C) and interaction with host rocks promote sulfide precipitation, which may lead to distal $Cu + Pb + Zn \pm Ag$ assemblages in vein and stockwork systems (e.g., Moore and Jackson, 1977; Mlynarczyk et al., 2003; Liu et al., 2016; Jiang et al., 2022; Leopardi et al., 2024).

At Sadisdorf (Germany), Pb–Zn sulfides (galena, sphalerite) occur in peripheral quartz–arsenopyrite–chalcopyrite veins, contrasting with proximal greisen-hosted Sn–W oxides; their mode of occurrence reflects fluid oxidation state and sulfur activity changes. Fluid inclusion data suggest mixing with meteoric water and decreasing salinity (0 wt %–10 wt % NaCl equiv.) in distal zones, facilitating base metal transport as chloride complexes and subsequent deposition via pH buffering (Leopardi et al., 2024). This zonation mirrors global greisen systems (e.g., San Rafael, Peru; Cligga Head, UK), where Pb–Zn mineralization marks the waning stages of hydrothermal activity, often overprinted by late fluorite–carbonate veins (Mlynarczyk et al., 2003; Moore and Jackson, 1977).

In Krupka, sulfide mineralization starts in the greisen stage, as evidenced by quartz–molybdenite veins with Sn–W mineralization (Knöttel deposit; Pauliš et al., 2022). The paragenetic sequence of sulfides (Žák, 1966) is very similar to that observed in Cínovec, starting with a sphalerite–chalcopyrite–pyrite assemblage followed by galena, Bi sulfides, and tennantite. The sulfide stage is followed by a final fluorite–carbonate stage with rare baryte. Krejčí Kotlánová et al. (2024) showed that the greisenization process took place at a temperature of 370–490 °C and a pressure of 155–371 bar, whereas the subsequent stages took place in a wide temperature range of < 120–370 °C. The source of fluids was not only magmatogenic but also meteoric water or fluids derived from sedimentary rocks.

A widely developed structural feature in the eastern Erzgebirge is the presence of flat-lying (subhorizontal) fractures, which are intensely mineralized with Sn–W–Li ores and associated sulfides. These structures are particularly well expressed in the Cínovec/Zinnwald cupola (e.g., Breiter et al., 2017b; Müller et al., 2018) and partly also in the Krupka district (Eisenreich and Breiter, 1993; Sejkora and Breiter, 1999; Pauliš et al., 2022). Their primary tectonic control is linked to the active exposure of granite intrusions, which promotes the formation of contractional fractures that broadly follow the morphology of the intrusion. Many of these subhorizontal fissures have been extensively exploited in the past and are notably enriched in Sn, W, Li, Cu, and Bi mineralization. These features collectively highlight the significance of contractional, intrusion-parallel structures for ore deposition in this segment of the Erzgebirge (David, 1991); the southern part of the Cínovec deposit, strongly dominated by massive greisens, represents an important anomaly.

Small vein-type mineral deposits combining cassiterite with common sulfides were historically mined in the central Erzgebirge; unfortunately, only basic mineralogical information is available. The W–E trending quartz veins at Hora svatého Šebestiána are located about 400 m above hidden peraluminous granite pluton and evolved in two stages: (1) quartz–cassiterite–chlorite and (2) quartz–cassiterite–sphalerite (with pyrrhotite, galena, chalcopyrite, tetrahedrite) (Breiter, 1981). About 20 NE- to SW-oriented veins were mined at Hora svaté Kateřiny. Mineralization evolved from the quartz–cassiterite stage and quartz–chlorite–sulfide stage (mainly sphalerite, chalcopyrite, and tetrahedrite) to, finally, the fluorite–carbonate stage (Breiter, 1982). The nearest outcrop of a rare-metal granite of type A was found ca. 1.5 km to the SW from the deposit (Breiter, 2008).

## 8 Conclusions

The world-class Li–Sn–W Cínovec deposit hosts base-metal sulfide mineralization composed mainly of Pb–Zn(–Cu) ores. Distribution of the sulfides at the deposit is irregular. Locally elevated but still subeconomic concentrations were found in the southern part of the deposit, mainly in its upper contact with the Teplice rhyolite. Sulfides are not strictly bound to prevalent Li–Sn–W mineralization. Their occurrence is constrained mainly by structural factors at the deposit. Progressive development of metal contents in the reduced sulfide-bearing hydrothermal fluid proceeds from Sn–Zn–Cu to Pb (Bi–Ag) and to As–Sb–Bi–Ag. Late-stage oxidized sulfate- and fluorine-bearing fluids partly altered earlier mineralization but did not deposit a significant amount of sulfide minerals. Complex mineral assemblages are a result of at least three metal-bearing fluid pulses (resulting in replace-

ment or dissolution of earlier minerals and precipitation of new phases) and a hydrothermal fluorite–baryte stage associated with low-temperature alteration. The spatial and genetic link of Li–Sn–W and sulfide mineralization is typical of the Erzgebirge and has multiple equivalents worldwide. The sulfide mineralization at the Cínovec Li–Sn–W greisen deposit seems to exhibit limited economic potential only due to low concentrations and irregular distribution. Sphalerite-dominated assemblages (Zn–Pb–Cu) have average grades of ∼ 100–200 ppm Zn (however, Zn is partly contained in zinnwaldite), 20–50 ppm Pb, and < 50 ppm Cu in disseminated mineralization, with locally elevated In contents (≤ 0.53 wt % in sphalerite). During the last stage of mining activity (1985–1990) in the southern part of the Cínovec deposit, recovered sulfides accounted for merely ∼ 13.9 g $t^{-1}$ of mined Li–Sn–W ore (ca. 2 kg per day was separated as a penalty material from the Sn–W sulfide concentrate produced by gravity separation; David, 1991). These bulk results do not match with locally high sulfide contents encountered in quartz–zinnwaldite veins in the central part of the cupola, mined for Sn and W in the past, represented in this study by the samples from the National Museum, Prague. Even though sulfide mineralization does not represent economic accumulation of minerals, it can serve as an important vector in the exploration of mineralized granites and other mineralization types (e.g., Pauliš et al., 2022; Sejkora et al., 2026) in the region.

**Data availability.** A list of studied samples and chemical data are available in the Supplement (Tables S1–13).

**Supplement.** The supplement related to this article is available online at https://doi.org/10.5194/ejm-38-281-2026-supplement.

**Author contributions.** The starting material was collected by OK and SH and from archives by LV, characterized by OK, JC, SH, and LV. Data collection, processing, and integration were performed by OK, JC, SH, JV, RŠ, LV, and ZD. The preparation of the paper was carried out by the whole research team.

**Competing interests.** The contact author has declared that none of the authors has any competing interests.

**Disclaimer.** Publisher's note: Copernicus Publications remains neutral with regard to jurisdictional claims made in the text, published maps, institutional affiliations, or any other geographical representation in this paper. The authors bear the ultimate responsibility for providing appropriate place names. Views expressed in the text are those of the authors and do not necessarily reflect the views of the publisher.

**Acknowledgements.** The authors thank Geomet s.r.o. for providing access to part of the study samples. We sincerely appreciate the valuable reviews provided by Tomáš Mikuš and an anonymous referee.

**Financial support.** This study received financial support from Geomet s.r.o (research project to Ondřej Krátký) under the framework of the Horizon Li4Life project (grant agreement no. 101137932 to Jan Cempírek) from the Ministry of Culture of the Czech Republic (long-term project DKRVO 2024–2028/1.I.c; National Museum, 00023272, to Luboš Vrtiška, Jiří Sejkora, and Zdeněk Dolníček) and from the Czech Academy of Sciences (project RVO 67985831 to Karel Breiter).

**Review statement.** This paper was edited by Rucheng Wang and reviewed by Tomáš Mikuš and one anonymous referee.

## References

Biagioni, C., George, L. L., Cook, N. J., Makovicky, E., Moëlo, Y., Pasero, M., Sejkora, J., Stanley, Ch. J., Welch, M., and Bosi, F.: The tetrahedrite group – Nomenclature and classification, Am. Miner., 105, 109–122, https://doi.org/10.2138/am-2020-7128, 2020.

Bindi, L., Evain, M., Spry, P. G., and Menchetti, S.: The pearceite-polybasite group of minerals: Crystal chemistry and new nomenclature rules, Am. Miner., 92, 918–925, https://doi.org/10.2138/am.2007.2440, 2007.

Bindi, L., Topa, D., and Keutsch, F. N.: How much copper can the pearceite structure sustain? The case of cupropearceite from Tsumeb, Namibia, Period. Mineral., 84, 341–350, https://doi.org/10.2451/2015PM0017, 2015.

Bonazzi, P., Bindi, L., Bernardini, G. P., and Menchetti, S.: A model for the mechanism of incorporation of Cu, Fe and Zn in the stannite-kësterite series, $Cu_2FeSnS_4$-$Cu_2ZnSnS_4$, Can. Mineral., 41, 639–647, 2003.

Bortnikov, N. S., Kudryavtsev, A. S., and Troneva, N. V.: Bi-rich tetrahedrite from the Tary-Ekan deposit East Karamazar, Central Asia, Mineralogiceskij Zhurnal, 198, 61–64, 1979.

Breiter, K.: Mineralization of the cassiterite-sulfidic formation of the Hora sv. Šebestiána in the Krušné Hory Mts., Acta Univ. Carol. Geol., 1981, 35–43, 1981 (in Czech with English abstract).

Breiter, K.: Minerogeneze ložiska kassiterit-sulfidické formace Hora sv. Kateřiny v Krušných horách, Zprávy a studie Krajského muzea v Teplicích, 15, 35–46, 1982.

Breiter, K.: Teplice rhyolite (Krušné hory Mts., Czech Republic) chemical evidence of a multiply exhausted stratified magma chamber, Věstník Českého geologického Ústavu, 72, 205–213, 1997.

Breiter, K.: Mineral and textural evolution of subvolcanic A-type granite: Hora Svaté Kateřiny stock, Krušné Hory Mts., Czech Republic, Z. geol. Wiss., 36, 365–382, 2008.

Breiter, K.: Nearly contemporaneous evolution of the A-type and S-type fractionated granites in the Krušné hory

– Erzgebirge Mts., Central Europe, Lithos, 151, 105–121, https://doi.org/10.1016/j.lithos.2011.09.022, 2012.

Breiter, K. and Škoda, R.: Vertical zonality of fractionated granite plutons reflected in zircon chemistry: the Cínovec A-type versus the Beauvoir S-type suite, Geol. Carpath., 63, 383–398, https://doi.org/10.2478/v10096-012-0030-6, 2012.

Breiter, K., Čopjaková, R., and Škoda, R.: The involvement of F, CO2, and As in the alteration of Zr–Th–REE-bearing accessory minerals in the Hora Svaté Kateřiny A-type granite, Czech Republic, Can. Mineral., 47, 1375–1398, https://doi.org/10.3749/canmin.47.6.1375, 2009a.

Breiter, K., Škoda, R., and Veselovský, F.: Unusual P-, Li- and Sn-rich pegmatite from Vernéřov near Aš, Czech Republic, Bulletin Mineralogicko-Petrologického Oddělení Národního Muzea v Praze, 17, 41–59, 2009b.

Breiter, K., Korbelová, Z., Šešulka, V., and Hönig, S.: New rock and mineral data from the Li–Sn–W–Nb–Ta deposit Cínovec-jih, Geoscience Research Reports, 49, 113–121, 2016.

Breiter, K., Ďurišová, J., and Dosbaba, M.: Quartz chemistry – A step to understanding magmatic-hydrothermal processes in ore-bearing granites Cínovec–Zinnwald Sn–W–Li deposit, Central Europe, Ore Geol. Rev., 90, 25–35, https://doi.org/10.1016/j.oregeorev.2017.10.013, 2017a.

Breiter, K., Ďurišová, J., Hrstka, T., Korbelová, Z., Hložková, M., Vašinová-Galiová, M., Kanický, V., Rambousek, P., Knésl, I., Dobeš, P., and Dosbaba, M.: Assessment of magmatic vs. metasomatic processes in rare-metal granites – a case study of the Cínovec–Zinnwald Sn–W–Li deposit, Central Europe, Lithos, 292–293, 198–217, https://doi.org/10.1016/j.lithos.2017.08.015, 2017b.

Breiter, K., Korbelová, Z., Chládek, V., Uher, P., Knésl, I., Rambousek, P., Hönig, S., and Šešulka, V.: Diversity of Ti–Sn–W–Nb–Ta oxide minerals in the classic granite-related magmatic–hydrothermal Cínovec–Zinnwald Sn–W–Li deposit, Czech Republic, Eur. J. Mineral., 29, 727–738, https://doi.org/10.1127/ejm/2017/0029-2650, 2017c.

Breiter, K., Galiová, M. V., Hložková, M., Korbelová, Z., Kynický, J., and Costi, H. T.: Trace element composition of micas from rare-metal granites of different geochemical affiliations, Lithos 446, https://doi.org/10.1016/j.lithos.2023.107135, 2023.

Burisch, M., Hartmann, A., Bach, W., Krolop, P., Krause, J., and Gutzmer, J.: Genesis of hydrothermal silver-antimony-sulfide veins of the Braunsdorf sector as part of the classic Freiberg silver mining district, Germany. Min. Dep., 54, 263–280, https://doi.org/10.1007/s00126-018-0842-0, 2019.

Buzatu, A., Damian, G., Dill, H. G., Buzgar, N., and Apopei, A. I.: Mineralogy and geochemistry of sulfosalts from Baia Sprie ore deposit (Romania) – New bismuth minerals occurrence, Ore Geol. Rev., 65, 132–147, https://doi.org/10.1016/j.oregeorev.2014.09.016, 2015.

Cháb, J., Breiter, K., Fatka, O., Hladil, J., Kalvoda, J., Šimůnek, Z., Štorch, P., Vašek, Z., Zajíc, J., and Zapletal, J.: Outline of the geology of the Bohemian Massif: the basement rocks and their Carboniferous and Permian cover, Czech Geological Survey Publishing House, Prague, 295 pp., 2010.

Cook, N. J.: Bismuth sulfosalts from hydrothermal vein deposits of Neogene age, N. W. Romania, Mitt. Österr. Mineral. Ges. 143, 19–39, https://doi.org/10.3390/min14111182, 1998.

David, J.: Final liquidation report Cínovec – south/Finální likvidační zpráva Cínovec – jih, unpublished report GF P103281, Czech Geological Survey, https://app.geology.cz/asgi/asg.php?item=1&tt_=D&asgid=194281 (last access: 1 January 2026), 1991 (in Czech).

Dolníček, Z., René, M., Prochaska, W., and Kovář, M.: Fluid evolution of the Hub Stock, Horní Slavkov–Krásno Sn–W ore district, Bohemian Massif, Czech Republic, Miner. Depos., 47, 821–833, 2012.

Dolníček, Z., Sejkora J., and Škácha, P.: Hypogene alteration of base–metal mineralization at the Václav vein (Březové Hory deposit, Příbram, Czech Republic): The result of recurrent infiltration of oxidized fluids, Minerals, 14, 1038, https://doi.org/10.3390/min14101038, 2024.

Eisenreich, M. and Breiter, K.: Krupka, deposit of Sn-W-Mo ores in the eastern Krušné hory Mts., Věstník Českého geologického ústavu, 68, 15–22, 1993.

Fontboté, L., Kouzmanov, K., Chiaradia, M., and Pokrovski, G. S.: Sulfide minerals in hydrothermal deposits, Elements, 13, 97–103, https://doi.org/10.2113/gselements.13.2.97, 2017.

Förster, H.-J. and Rhede, D.: The Be–Ta-rich granite of Seifen (Eastern Erzgebirge, Germany): accessory mineral chemistry, composition and age of a late-Variscan Li–F granite of A-type affinity, Neues Jb. Miner. Abh., 182, 307–321, https://doi.org/10.1127/0077-7757/2006/0055, 2006.

Förster, H. J., Rhede, D., and Tischendorf, G.: Mineralogy of the Niederschlema-Alberoda U-Se-polymetallic deposit, Erzgebirge, Germany. I. Jolliffeite, NiAsSe, the rare Se-dominant analogue of gersdorffite, Can. Min., 42, 841–849, https://doi.org/10.2113/gscanmin.42.3.841, 2004.

Förster, H.-J., Gottesmann, B., Tischendorf, G., Siebel, W., Rhede, D., Seltmann, R., and Wasternack, J.: Permo-Carboniferous subvolcanic rhyolitic dikes in the western Erzgebirge/Vogtland, Germany: a record of source heterogeneity of post-collisional felsic magmatism, Neues Jb. Miner. Abh., 183, 123–147, 2007.

Gołębiowska, B., Pieczka, A., and Parafiniuk, J.: Substitution of Bi for Sb and As in minerals of the tetrahedrite series from Rdziny, Lower Silesia, southwestern Poland, Can. Mineral., 50, 267–279, https://doi.org/10.3749/canmin.50.2.267, 2012.

Hoth, K., Wasternack, J., Berger, H. J., Breiter, K., Mločoch, B., and Schovánek, P.: Geologische Karte Erzgebirge / Vogtland (2. Aufl), Freiberg: Sächsisches Landesamt für Umwelt und Geologie, Bereich Boden und Geologie, https://www.archiv.sachsen.de/archiv/bestand.jsp?guid=7cfc80f9-12df-4da7-ba9f-7cb1868c16f7 (last access: 7 May 2026), 1995.

Hreus, S., Výravský, J., Cempírek, J., Breiter, K., Vašinová, G., Krátký, O., Šešulka, V., and Škoda, R.: Scandium distribution in the world-class Li-Sn-W Cínovec greisen-type deposit: Result of a complex magmatic to hydrothermal evolution, implications for scandium valorization, Ore Geol. Rev., 134, 104433, https://doi.org/10.1016/j.oregeorev.2021.104433, 2021.

Hrstka, T., Gottlieb, P., Skála, R., Breiter, K., and Motl, D.: Automated mineralogy and petrology-applications of TESCAN Integrated Mineral Analyzer (TIMA), J. Geosci., 63, 47–63, https://doi.org/10.3190/jgeosci.250, 2018.

Jiang, H., Jiang, S. Y., Li, W. Q., Zhao, K. D., Zhang, W., and Zhang, Q.: Genesis of the Hermyingyi W–Sn deposit, southern Myanmar, SE Asia – Constraints from fluid inclusion and mul-

tiple isotope (C, H, O, S, and Pb) studies, Miner. Depos., 577, 1211–1226, https://doi.org/10.1007/s00126-022-01099-y, 2022.
Johan, V. and Johan, Z.: Accessory minerals of the Cínovec–Zinnwald granite cupola, Czech Republic – Part 1 Nb–, Ta– and Ti–bearing oxides, Mineral. Petrol., 51, 323–343, https://doi.org/10.1007/BF01159735, 1994.
Johan, Z. and Johan, V.: Accessory minerals of the Cínovec (Zinnwald) granite cupola, Czech Republic: indicators of petrogenetic evolution, Mineral. Petrol., 83, 113–150, https://doi.org/10.1007/s00710-004-0058-0, 2005.
Kieft, K. and Eriksson, G.: Regional zoning and metamorphic evolution of the Vindfall Pb–Zn ore, east central Sweden, Geol. Fören. Stock. För., 106, 305–317, https://doi.org/10.1080/11035898509454655, 1984.
Kissin, S. A.: A re-investigation of the stannite ($Cu_2FeSnS_4$) – kesterite ($Cu_2ZnSnS_4$) pseudobinary system, Can. Mineral., 27, 689–697, 1989.
Kissin, S. A. and Owens, D. A. R.: The relatives of stannite in the light of new data, Can. Mineral., 27, 673–688, 1989.
Kondela, J., Hreus, S., Tóth, S., and Farkašovský, R.: Hydrothermal quartz veins with Bi-bearing sulfidic mineralization and Bi-tellurides at the Gemerská Poloma talc deposit, Spišsko-gemerské rudohorie Mts., Slovakia, Mineral. Petrol., 1–22, https://doi.org/10.1007/s00710-025-00898-1, 2025.
Korges, M., Weis, P., Lüders, V., and Laurent, O.: Depressurization and boiling of a single magmatic fluid as a mechanism for tin–tungsten deposit formation, Geology, 461, 75–78, https://doi.org/10.1130/G39601.1, 2018.
Kotková, J., O'Brien, P. J., and Ziemann, M. A.: Diamond and coesite discovered in Saxony-type granulite: Solution to the Variscan garnet peridotite enigma, Geology, 39, 667–670, https://doi.org/10.1130/G31971.1, 2011.
Krejčí Kotlánová, M., Dolníček, Z., René, M., Prochaska, W., Ulmanová, J., Kapusta, J., Mašek, V., and Kropáč, K.: Fluid evolution of greisens from Krupka Sn–W ore district, Bohemian Massif (Czech Republic), Minerals, 14, 86, https://doi.org/10.3390/min14010086, 2024.
Leopardi, D., Gutzmer, J., Lehmann, B., and Burisch, M.: The spatial and temporal evolution of the Sadisdorf Li–Sn–(W–Cu) magmatic–hydrothermal greisen and vein system, Eastern Erzgebirge, Germany, Econ. Geol., 119, 771–804, https://doi.org/10.5382/econgeo.5077, 2024.
Linnemann, U.: Das Saxothuringikum, Dresden, 163 pp., 2008.
Linnemann, U. and Romer, R. L.: Pre-Mesozoic geology of Saxo-Thuringia from the Cadomian active margin to the Variscan orogen, Schweizerbart, Stuttgart, 485 pp., 2010.
Liu, Y., Jiang, S., and Bagas, L.: The genesis of metal zonation in the Weilasituo and Bairendaba Ag–Zn–Pb–Cu–Sn–W deposits in the shallow part of a porphyry Sn–W–Rb system, Inner Mongolia, China., Ore Geol. Rev., 75, 150–173, https://doi.org/10.1016/j.oregeorev.2015.12.006, 2016.
Lowry, D., Stephens, W. E., Herd, D. A., and Stanley, C. J.: Bismuth sulfosalts within quartz veining hosted by the Loch Shin monzogranite, Scotland, Mineral. Mag., 58, 39–47, https://doi.org/10.1180/minmag.1994.058.390.04, 1994.
Makovicky, E.: Algorithms for calculations of homologue order N in the homologous series of sulfosalts, Eur. J. Mineral., 31, 83–97, https://doi.org/10.1127/ejm/2018/0030-2791, 2019.
Makovicky, E. and Makovicky, M.: Representation of compositions in the bismuthinite–aikinite series, Can. Mineral., 16, 405–409, 1978.
Mederski, S., Pršek, J., Kołodziejczyk, J., Kluza, K., Melfos, V., Adamek, K., and Dimitrova, D.: Mineralogical and geochemical studies of Cu-Bi-Ag ± W ores from Janjevo (Kosovo): Insights into the Bi sulfosalt mineralogy and the distribution of bismuth in base metal sulfides, J. Geosci., 68, 139–162, https://doi.org/10.3190/jgeosci.371, 2023.
Merlet, C.: An accurate computer correction program for quantitative electron probe microanalysis, Microchim. Acta, 114, 363–376, https://doi.org/10.1007/BF01244563, 1994.
Mlynarczyk, M. S. J., Sherlock, R. L., and Williams-Jones, A. E.: San Rafael, Peru – Geology and structure of the world's richest tin lode, Miner. Depos., 385, 555–567, https://doi.org/10.1007/s00126-002-0334-z, 2003.
Moëlo, Y., Makovicky, E., Mozgova, N. N., Jambor, J. L., Cook, N., Pring, A., Paar, W., Nickel, E. H., Graeser, S., Karup-Møller, S., Balić-Žunić, T., Mumme, W. G., Vurro, F., Topa, D., Bindi, L., Bente, K., and Shimizu, M.: Sulfosalt Systematics: A Review Report of the Sulfosalt Sub-Committee of the IMA Commission on Ore Mineralogy, Eur. J. Mineral., 20, 7–46, 2008.
Moore, J. and Jackson, N.: Structure and mineralization in the Cligga granite stock, Cornwall, J. Geol. Soc., 335, 467–480, https://doi.org/10.1144/gsjgs.133.5.0467, 1977.
Müller, A., Breiter, K., Seltmann, R., and Pécskay, Z.: Quartz and feldspar zoning in the eastern Erzgebirge volcano-plutonic complex (Germany, Czech Republic): evidence of multiple magma mixing, Lithos, 80, 201–227, 2005.
Müller, A., Herklotz, G., and Giegling, H.: Chemistry of quartz related to the Zinnwald–Cínovec Sn–W–Li greisen-type deposit, Eastern Erzgebirge, Germany, J. Geochem. Explor., 190, 357–373, https://doi.org/10.1016/j.gexplo.2018.04.009, 2018.
Novák, F., Jansa, J., and David, J.: Roquesite from the Sn-W deposit of Cínovec in the Krušné Hory Mts. (Czechoslovakia), Věstník Ústředního ústavu geologického, 66, 3, 173–181, 1991.
Pauliš, P., Dvořák, Z., Babka, K., and Fuchs, P.: Nerostné bohatství Krupky, Cínovce a Moldavy, Martin Bartoš (Kuttna), Kutná Hora, ISBN 978-80-86406-96-1, 2022.
Pósfai, M. and Buseck, P. R.: Relationships between microstructure and composition in enargite and luzonite, Am. Miner., 83, 373–382, https://doi.org/10.2138/am-1998-3-422, 1998.
Pouchou, J. L. and Pichoir, F.: Détermination par microanalyse X de l'épaisseur et de la composition de couches minces superficielles, J. Microsc. Spectrosc. Electron., 10, 279, 1985.
Ramdohr, P.: The ore minerals and their intergrowth, 2nd ed. (English ed. of the 4th German edition, with additions and corrections by the author), Pergamon Press, Oxford, 1205 pp., 1980.
Romer, R. L., Thomas, R., Stein, H. J., and Rhede, D.: Dating multiply overprinted Sn-mineralized granites – examples from the Erzgebirge, Germany, Miner. Depos., 42, 337–359, 2007.
Schorr, S., Hoebler, H.-J., and Tovar, M.: A neutron diffraction study of the stannite-kesterite solid solution series, Eur. J. Mineral., 19, 65–73, 2007.
Sejkora, J. and Breiter, K.: Historický rudní revír Krupka, Krušné hory, Bulletin Mineralogicko-Petrologického Oddělení Národního Muzea v Praze, 7, 29–45, 1999.
Sejkora, J., Škácha, P., Kopecký Sr., S., Kopecký Jr., S., Pauliš, P., Malíková, R., and Velebil, D.: Se and Cu mineraliza-

tion from Bílá Voda near Javorník, Czech Republic, Bulletin Mineralogicko-Petrologického Oddělení Národního Muzea v Praze, 24, 161–177, 2016.

Sejkora, J., Pauliš, P., Urban, M., Dolníček, Z., Ulmanová, J., and Pour, O.: Mineralogie křemenných žil ložiska cínových rud Hřebečná u Abertam v Krušných horách (Česká republika), Bulletin Mineralogie Petrologie, 29, 131–163, https://doi.org/10.46861/bmp.29.131, 2021.

Sejkora, J., Biagioni, C., Dolníček, Z., Velebil, D., and Škácha, P.: Annivite-(Zn), $Cu_6(Cu_4Zn_2)_{\Sigma 6}Bi_4S_{13}$, from the Jáchymov ore district, Czech Republic: the first Bi-dominant member of the tetrahedrite group, Mineral. Mag., 89, 102–112, https://doi.org/10.1180/mgm.2024.54, 2025.

Sejkora, J., Plášil, J., Makovicky, E., Škácha, P., Dolníček, Z., and Gramblička, R.: Argentopearceite, $Ag_{16}As_2S_{11}$, a new silver mineral from the Mikulov and Moldava deposits, (Czech Republic), Mineral. Mag., 90, 21–32, https://doi.org/10.1180/mgm.2025.10101, 2026.

Skinner, B. J.: Thermal expansion, in: Handbook of Physical Constants, edited by: Clark Jr., S. P., Geol. Soc. Am. Mem., 97, 75–96, https://doi.org/10.2113/gsecongeo.61.1.1, 1966.

Spiridonov, E. M., Chvileva, T. N., Borodaev, Y. S., Vinogradova, R. A., and Kononov, O. V.: The influence of bismuth on optical properties of gray copper, Dokl. Akad. Nauk SSSR, 290, 1475–1478, 1986.

Staude, S., Dorn, A., Pfaff, K., and Markl, G.: Assemblages of Ag-Bi sulfosalts and conditions of their formation: The type locality of schapbachite (Ag0.4Pb0.2Bi0.4S) and neighboring mines in the Schwarzwald ore district, southern Germany, Can. Min., 48, 441–466, https://doi.org/10.3749/canmin.48.3.441, 2010.

Štemprok, M.: Sulfidische Vererzung auf der Erzlagerstätte Cínovec–Zinnwald im Erzgebirge, Sborník Ústředního Ústavu geologického, 27, 7–57, 1962.

Štemprok, M.: Final liquidation report Cínovec-veins, Appendix No. 14 Minerogenesis of the Cínovec ore deposit/Závěrečná likvidační zpráva Cínovec-žíly, Příloha č.14 Minerogenese rudního ložiska Cínovec, unpublished report GF P103112, Czech Geological Survey, 328 pp., https://app.geology.cz/asgi/asg.php?item=1&tt_=D&asgid=194112 (last access: 1 January 2026), 1987 (in Czech).

Štemprok, M. and Šulcek, Z.: Geochemical profile through an ore-bearing lithium granite, Econ. Geol., 64, 392–404, https://doi.org/10.2113/gsecongeo.64.4.392, 1969.

Ševko, M. and Sejkora, J.: Bismuth, lead–bismuth and lead–antimony sulfosalts from the granite-hosted hydrothermal quartz veins at the Elisabeth mine, Gemerská Poloma, Spišsko-gemerské rudohorie Mts., Slovakia, J. Geosci., 66, 157–173, https://doi.org/10.3190/jgeosci.328, 2021.

Tichomirowa, M., Käßner, A., Sperner, B., Lapp, M., Leonhardt, D., Linnemann, U., Münker, C., Ovtcharova, M., Pfänder, J. A., and Schaltegger, U.: Dating multiply overprinted granites: The effect of protracted magmatism and fluid flow on dating systems (zircon U–Pb: SHRIMP/SIMS, LA-ICP-MS, CA-ID-TIMS and Rb–Sr, Ar–Ar) – Granites from the Western Erzgebirge (Bohemian Massif, Germany), Chem. Geol., 519, 11–38, https://doi.org/10.1016/j.chemgeo.2019.04.024, 2019.

Tichomirowa, M., Kässner, A., Repstock, A., Weber, S., Gerdes, A., and Whitehouse, M.: New CA-ID-TIMS U–Pb zircon ages for the Altenberg–Teplice Volcanic Complex (ATVC) document discrete and coeval pulses of Variscan magmatic activity in the Eastern Erzgebirge (Eastern Variscan Belt), Int. J. Earth Sci., 111, 19, https://doi.org/10.1007/s00531-022-02204-2, 2022.

Tomek, F., Žák, J., Svojtka, M., Finger, F., and Waitzinger, M.: Emplacement dynamics of syn-collapse ring dikes: An example from the Altenberg-Teplice caldera, Bohemian Massif, GSA Bulletin, 131, 997–1016, https://doi.org/10.1130/B35019.1, 2019.

Topa, D., Makovicky, E., and Paar, W. H.: Composition ranges and exsolution pairs for the members of the bismuthinite–aikinite series from Felbertal, Austria, Can. Mineral., 40, 849–869, https://doi.org/10.2113/gscanmin.40.3.849, 2002.

Topa, D., Makovicky, E., Putz, H., and Mumme, W. G.: The crystal structure of berryite, $Cu_3Ag_2Pb_3Bi_7S_{16}$, Can. Mineral., 44, 465–480, https://doi.org/10.2113/gscanmin.44.2.465, 2006.

Velebil, D. and Sejkora, J.: Bi-rich tennantites from Jáchymov, Czech Republic, Bulletin Mineralogie Petrologie, 26, 213–222, 2018.

Vlasáč, J., Mikuš, T., Majzlan, J., Ševko, M., Biroň, A., Szczerba, M., Milovský, R., and Žitňan, P.: Mineralogy and evolution of the epithermal mineralization in the Rudno nad Hronom – Brehy ore deposit, Štiavnické vrchy Mts. (Slovakia), J. Geosci., 69, 21–47, 2024.

Warr, L. N.: IMA–CNMNC approved mineral symbols, Mineral. Mag., 85, 329–320, https://doi.org/10.1180/mgm.2021.43, 2021.

Weber, S., Legler, C., Kallmeier, E., Schulz, B., and Burisch, M.: Metamorphic origin of stratiform cassiterite mineralization in the Schwarzenberg–Aue district – Clues to the metamorphic history and pre–orogenic Sn enrichment of the Erzgebirge, Germany, Lithos, 454–455, 107014, https://doi.org/10.1016/j.lithos.2023.107273, 2023.

Yamanaka, T. and Kato, A.: Mössbauer effect study of $^{57}$Fe and $^{119}$Sn in stannite, stannoidite, and mawsonite, Am. Miner., 61, 260–265, 1976.

Žák, L.: Origin of the molybdenite and feldspar deposit of Krupka in the Krušné hory Mts. II. Paragenetic relations, Acta Universatis Carolinae, Geologica, 3, 167–195, 1966.